Institute for Functional Matter and Quantum Technologies
University of Stuttgart, Germany
Pfaffenwaldring 57, 70550 Stuttgart

MD Simulations of 3D Laser Printing

Master Thesis: Jonas Schmid

Examiner: Prof. Dr. Johannes Roth
Co-Examiner: Prof. Dr. Christian Holm

February 2024

Abstract

In this thesis, a simulation framework for powder bed fusion using molecular dynamics is developed. The goal is to study the melting and solidification of an aluminum powder and to create a framework that allows for further studies on arbitrary alloys and metals. Molecular dynamics leads to an understanding of the melting and ablation process, resulting in an understanding of different heat transfer mechanisms. The influence of a change in scanning speed and laser power on the melting dynamics is accessible with the simulation framework. Furthermore, the cooling of the sample leads to an explicit understanding of nucleation and grain growth. Structural properties such as grain size and gas inclusions can be studied as a function of laser parameters, powder composition and cooling rate. For the recrystallized sample, mechanical properties are determined to investigate the influence of lattice structure and gas inclusions. With these properties modeled at the atomistic scale, this work attempts to link the methods from laser ablation simulations with the powder bed fusion process. The results from molecular dynamics simulations are intended to complement results from larger finite element simulations by providing numerous properties at the atomistic scale.

Contents

Abbreviations

AM	Additive Manufacturing
PBF	Powder Bed Fusion
SLS	Selective Laser Sintering
MD	Molecular Dynamics
FEM	Finite Element Method
IMD	ITAP Molecular Dynamics program
EAM	Embedded Atom Model
PBC	Periodic Boundary Conditions
FCA	Free Carrier Absorption
NH	Nosé-Hoover Thermostat
TTM	Two Temperature Model
CNA	Common Neighbor Analysis
FWHM	Full Width Half Max
FCC	Face-Centered Cubic
HCP	Hexagonal Close-Packed

Chapter 1

Introduction

Additive manufacturing (AM) is on the rise, and not just because of the continued increase in cost efficiency and decrease in production time [1]. Traditional manufacturing techniques are limited when it comes to complex geometries and intricate internal structures of components [2]. Many aerospace components take advantage of AM manufacturing. Complex internal structures can be used to reduce weight or incorporate internal cooling channels. Examples include rocket nozzles and liquid oxygen pumps [3]. AM is also opening up new fields: custom-printed bicycle frames that allow millimeter-perfect sizing and combine stiffness with aerodynamic gains [4]. The wide range of accessible fields results from the numerous advantages of the different AM processes.

While AM, or 3D printing in general, is mostly associated with the printing of polymers, due to similar advantages, the printing of metals and alloys is becoming increasingly relevant in commercial applications. In this context, laser-induced AM processes such as powder bed fusion (PBF) and selective laser sintering (SLS) are becoming relevant due to the high density of materials, including polymers, metal alloys and ceramics. In particular, PBF can provide fully dense metal parts with excellent mechanical properties. In addition, PBF provides precise control over the composition of the manufactured component [5]. Due to the one-step production process, PBF is suitable for prototyping, despite a change in the processed material or the size of the component, no tooling is generally required [6].

Besides the advantages, there are still some challenges and limitations to be faced. Despite the high cost of equipment and infrastructure associated with PBF [7], the main challenge consists of quality control and reproducibility [8].

To optimize the experimental design of the process and address these challenges, simulations of the process can provide insight into specific experimental parameters. Simulations have several advantages over experimental testing of a set of parameters. On the one hand, testing a set of parameters in a simulation reduces material waste as well as the cost of the process in general, while on the other hand, the iteration step of changing parameters in a simulation is shorter and less labor-intensive compared to changing an experimental setup [9]. In addition to the efficiency advantages, simulation also provides some advan-

tages in understanding the process. While an experimental setup provides only the final component, a simulation allows a closer look at the process itself, providing information on the origin of the component's properties. Structural properties of a sample are also more accessible in a simulation.

In order to access the microstructural behavior of the fabricated sample, the simulations are performed using molecular dynamics (MD). The simulations are performed using the ITAP Molecular Dynamics program (IMD), which allows efficient computation of large-scale simulations on an atomistic basis [10]. The simulation of PBF is based on the laser ablation work of Dominic Klein [11]. Atomistic simulation allows the observation of structural properties on an atomistic basis. It also requires fewer assumptions about the sample than finite element modeling (FEM). The limitations of the sample size lead to customized parameters in the MD simulation to model the process and obtain applicable results for FEM simulations and experimental applications.

Chapter 2

Background

This chapter deals with the background of the underlying manufacturing process, the implementation of the simulation and the physical background.

While there are several AM processes besides PBF, an overview of the currently most relevant AM processes is given in section 2.1. The specific PBF process is explained in section 2.1.1, followed by a discussion of the process properties of the laser (section 2.1.2), the powder (section 2.1.3), and the resulting sample (section 2.1.4).

In section 2.2, the framework of MD simulations and the physical background are outlined. Further, the implementation of the MD simulation as well as some optimization methods are mentioned. Since the laser-powder interaction plays a crucial role in the simulation, the implementation of the interaction is described in section 2.3.

In order to interpret the simulations and in particular to obtain properties that can only be observed in MD simulations, simulation and analysis tools are described in section 2.4.

2.1 Additive Manufacturing

There are various advantages to AM processes as pointed out in chapter 1, there are several AM processes with different applications. The oldest AM technique is stereolithography, in which a liquid polymer resin is selectively cured by an ultraviolet laser. This process produces detailed parts with smooth surfaces, but is severely limited by the material being manufactured [12]. Very similar to this process is material jetting, where droplets of material are deposited onto the underlying sample and cured with UV light. This technique has the advantage of building multi-material parts [13]. Fused Deposition Modeling is the most widely used manufacturing technique for home use. A heated filament is extruded through a nozzle that distributes the filament over the previous layer. The filament hardens due to cooling [14]. The binder jetting process is similar to the PBF process described below fig. 2.1(a). The difference is that the powder is bonded together by spreading a binder onto the top layer of powder [15].

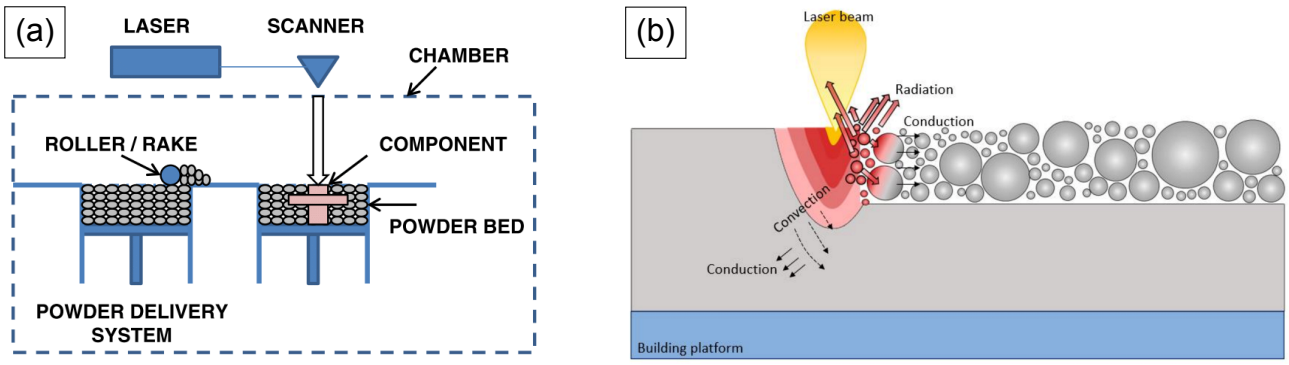

Figure 2.1: A general PBF process is Illustrated in (a) [16]. The melting behavior of the powder induced by the laser beam is shown in (b) [17].

2.1.1 Powder Bed Fusion (PBF) Manufacturing Process

This work deals with the PBF process, we will have a closer look into the procedure as well as the experimental realization and the current applications.

The layer-by-layer fabrication process of PBF is shown in fig. 2.1(a). For each layer, metal powder is deposited from the powder delivery system onto the pre-printed sample using, for example, a roller. Therefore, the sample is the previously printed sample is lowered after each melting process. After the new powder has been distributed on the sample, a new layer is melted onto the already printed component. The melting process is initiated by a laser, while a scanner moves the laser spot according to the desired structure of the component. Typically, the melting process takes place in a chamber filled with a protective gas such as argon or another novel gas to prevent the metal powder from oxidizing during melting.

A schematic of the powder melting process is shown in fig. 2.1(b). The goal of the melting process is to melt the entire powder layer at the top, as well as parts of the previously printed layer underneath. The energy induced by the laser is distributed through the sample by thermal conduction, particle convection, and laser radiation. Depending on the heat transfer mechanism caused by the laser and the powder properties, the melting behavior as well as the laser reflection differs [18].

The same process is used for SLS. In this process, the powder is heated to a temperature just below the melting point, which causes sintering onto the previous layer. The SLS manufacturing process, in contrast to PBF, generally requires different processes as a consequence of the inevitable porosity and the need for sintered support structures [19]. The simulation of SLS is also not applicable to the nanoscale. Due to the surface to volume ratio, the sintering process takes place at room temperature. Further investigations on the nanoscale are prepared in [20] using a niobium-zirconium alloy powder, while the overall dynamics can be compared to the aluminum nanospheres.

2.1.2 Laser Properties

To understand the melting process in detail, the interaction between the laser and the metal powder plays a crucial role. The interaction at the atomic and subatomic scale is discussed in section 2.3.2. In this section, macroscopic and experimental laser properties and their influence on the melting process are mentioned [21].

The carbon dioxide laser (CO_2) and the Nd:YAG laser are commonly used in the PBF process due to their high power output. The laser energy is distributed in a Gaussian shape, while the penetration can be done by pulsed interaction or continuous melting [21]. In the experiment, laser beams of the size down to less then $25\,\mu m$ are realizable [22]. The laser power is in the range of $50\,$W up to the order of kW, depending on the scanning speed in the order of mm$/$s and the beam size [21]. The scaling of laser parameters is discussed in section 4.1.2.

Melting dynamics depend mostly on the laser power and the associated scan speed. A general overview of the relationship between laser power and laser scan speed is shown in fig. 2.2. High laser powers and low laser speeds result in rapid vaporization of the solid. While the gas expands rapidly, liquid portions of the metal are displaced. this convective behavior leads to keyhole formation, which causes unwanted porosity in the sample. Low laser power and fast scan speeds lead to a lack-of-fusion regime, simply due to an insufficient amount of energy absorbed by the sample [23]. At high laser power combined with low scan speed, the Rayleigh instability plays a critical role in the melting process due to the large keyhole depth. If the length of the keyhole is much larger than its diameter, the Rayleigh instability will cause the keyhole to close, resulting in fragmentation into multiple smaller inclusions. When a keyhole is closed, the laser interacts strongly with the closing part of the keyhole due to laser reflection. This causes the keyhole to oscillate, resulting in large welding defects [24].

The reproduction of keyholing, and in particular the oscillation of the keyhole, using MD simulations presents many difficulties. The reluctance within the sample plays a crucial role in keyhole formation. MD does not generically provide a defined surface to calculate the reflections of the laser at the surface of the sample. In addition, the surface tension of the liquid metal is essential for the stability of the pore, while the minimum size required is of the order of μm, which is larger than the size modeled in MD simulations.

In addition to the general melting behavior, the ablation depth plays an important role in the selection of suitable laser parameters. In order to obtain a sample with robust mechanical properties, the goal is not only to melt the current powder layer, but also to remelt the previous layer underneath. The dependency between laser fluence and ablation depth has finally been clarified. While different experimental setups mostly show a linear relationship between laser fluence and ablation depth [25] [26] [27].

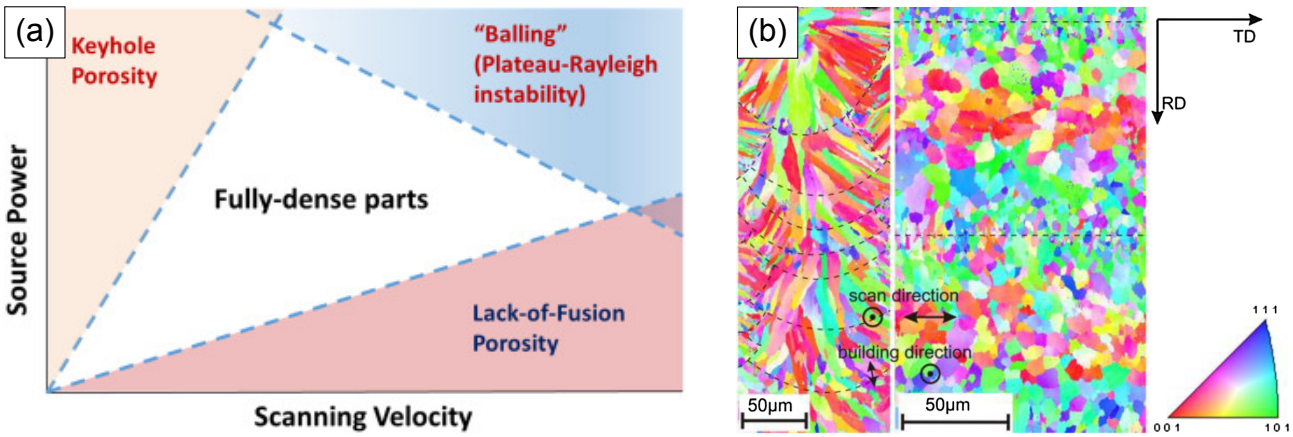

Figure 2.2: A general illustration of the influence of the laser parameters on the melting behavior and the sample characteristics is shown in (a) [23]. Figure (b) shows an Electron Backscatter Diffraction image of an PBF sample using AlSi10Mg, whereas the anisotropic nature of PBF manufactured parts is shown [28].

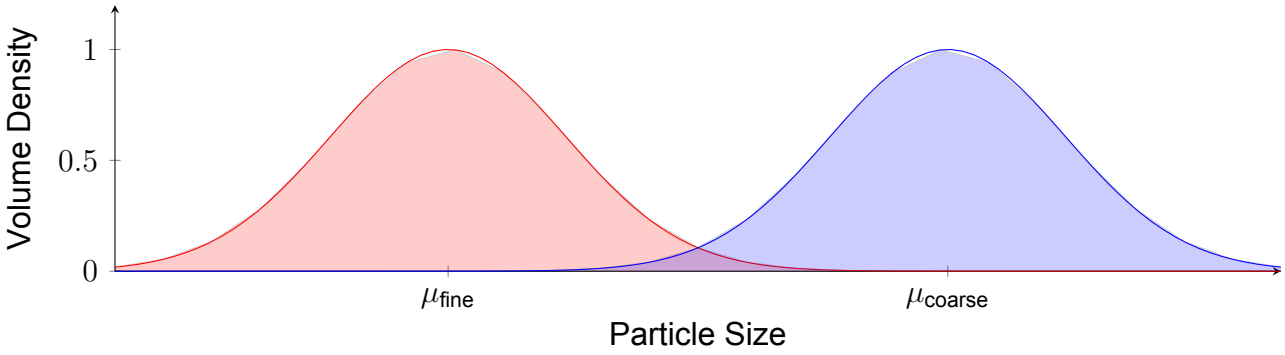

Figure 2.3: General illustration of size distribution of a powder consisting of two Gaussian distributions with the mean μ_{Fine} and μ_{Coarse}

2.1.3 Powder Properties

Another important property in the PBF process is the composition of the metal powder and its configuration prior to the start of the melting process. In experimental setups, the powder consists of a distribution of grain sizes. The production of the powder results in a Gaussian distribution for the size of the powder grains [29]. In order to achieve a higher packing density of the powder, which empirically results in a reduction of gas pockets, the size distribution of the powder consists of two or several [30] Gaussian distributions. An example of a powder distribution composed of two Gaussian distributions is shown in fig. 2.3.

2.1.4 Sample Properties

The powder and laser properties cause defects in the resulting part that must be addressed to produce a high-strength part. The main defects in PBF parts are porosity, pore formation, anisotropy in the lattice structure and surface roughness. An example of a lack-of-fusion defect is shown in fig. 2.4(b), where incompletely melted powder grains lead to whole grains in the resulting sample. A complete melting of the powder as well as a partial melting

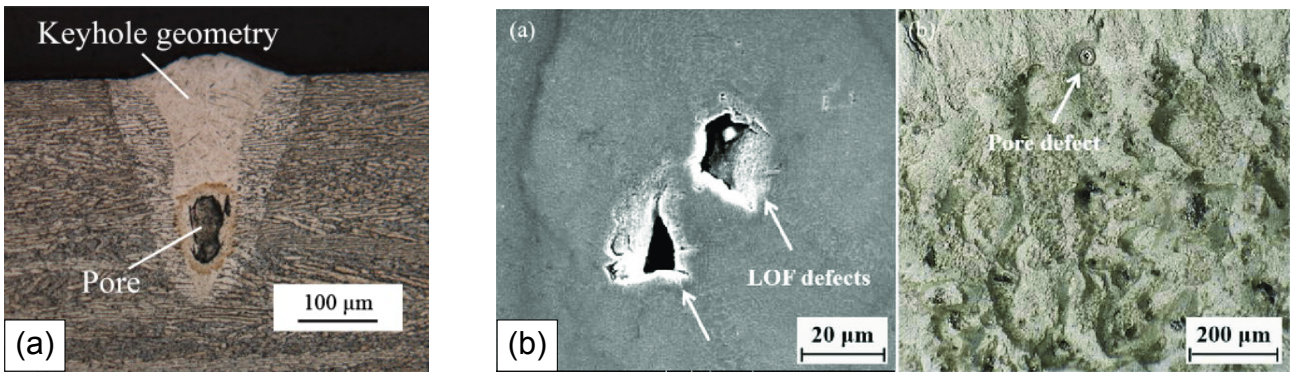

Figure 2.4: (a) Cross section of a keyhole with a pore [32]. (b) Surface pictures of lack of fusion defects as well as a pore formation [33].

of the sample is shown in [31]. Lack of fusion, fusion, and the formation of pores due to very high laser power degrade the mechanical properties of the sample. The shape of a pore formed as a result of a keyhole during melting is shown in fig. 2.4(a). The pore formation during the recrystallization of the sample, the formation of grain structure in unavoidable. Different lattice orientations of the epitaxially growing grains lead to an anisotropic sample structure as shown in fig. 2.2(b). Other grain structures produced by PBF in the direction of growth are defined by the expansion of the melt top, showing the radial epitaxial growth of lattice structures (see fig. 2.2(b)).

2.2 Molecular Dynamics

To select an appropriate simulation setup to model PBF, one must define the intent of the simulation as well as the computational resources. In industry, the manufacturing of a component with a size in the range of millimeters to centimeters is most relevant. The preferred simulation tool for this application is the Finite Element Method (FEM). While the results of these simulations can be validated with the experiment [34] and require a reasonable amount of computational resources compared to the size of the component, FEM has many limitations. FEM simulations provide little information about the melting process itself. Physical properties such as lattice structure and crack or droplet formation are just consequences of assumptions made externally to the simulation. In order to gain a deeper insight into the PBF process itself and to observe microscopic energy and structure properties, MD simulations are used in this work.

In MD simulations, the trajectory of each atom is calculated separately by solving Newton's equations. The change in momentum of atom i is thus given by

$$\frac{\mathrm{d}\mathbf{p}_i}{\mathrm{d}t} = \mathbf{F}_i(\{\mathbf{x}\}) \text{ with } \frac{\mathrm{d}\mathbf{x}_i}{\mathrm{d}t} = \frac{1}{m_i}\mathbf{p}_i. \tag{2.1}$$

The force $\mathbf{F}_i(\{\mathbf{x}\})$ describes the interaction force that all other atoms in the system exert on atom i. While the force $\mathbf{F}_i(\{\mathbf{x}\})$ can depend on all initial atom positions, we get a system of coupled differential equations whose dimension is given by the number of particles in the system. While there is no closed-form solution for coupled Newton equations for three or more particles, one must approximate the Newton equations (2.1) numerically. Therefore, we simply compute the atomic positions $\{\mathbf{x}\}$ in discrete intervals Δt_{MD}. In an MD step, the state of the system at time $t + \Delta t_{\mathrm{MD}}$ is calculated from the state of the system at time t. An example of an MD step for two attracting particles is shown in fig. 2.5. There are two atoms at the coordinates $\mathbf{x}_1$ and $\mathbf{x}_2$ with the velocities $\mathbf{v}_1$ and $\mathbf{v}_2$ at the time t and they exert the force $\mathbf{F}_{ij}(\{\mathbf{x}\}$ depending on their animistic interaction. A numerical integration calculates the new coordinates $\mathbf{x}'_1$ and $\mathbf{x}'_2$ with the new velocities $\mathbf{v}'_1$ and $\mathbf{v}'_2$ at time $t + \Delta t_{\mathrm{MD}}$. This step is repeated by now applying $\mathbf{F}'_{ij}(\{\mathbf{x}'\})$ to the system. The results and the computational effort of the MD simulation do not only depend on the chosen time step Δt_{MD}. The chosen numerical integrator as well as the calculation of the force $\mathbf{F}_i(\{\mathbf{x}\})$ play a crucial role in the simulation.

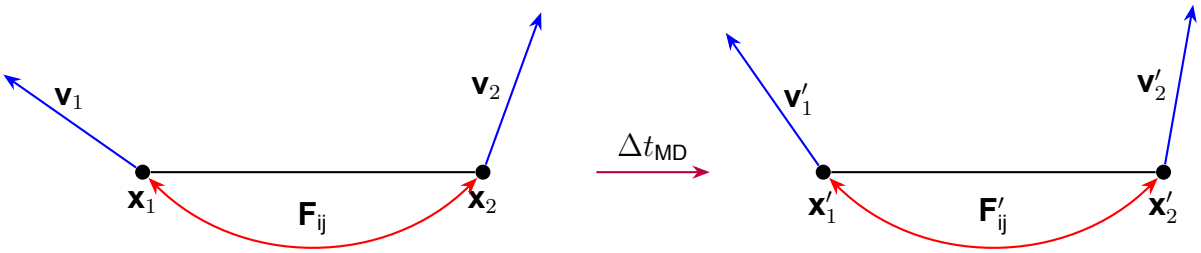

Figure 2.5: Example for an MD step of two attraction atoms.

2.2.1 Integrators

The step of numerical integration in an MD simulation is to calculate the trajectory of a particle responsible for the thermodynamic ensemble with which the system should be modeled.

The **Microcanonical Ensemble** describes a system without interaction with an external heat bath. Consequently, the integrator must conserve energy and produce time reversal trajectories. Integrators that perform canonical transformations are called symplectic. In our simulation, we use the leapfrog algorithm [35], which performs a second order numerical integration. The coordinate $\mathbf{x}_i(t + \delta t_{\mathsf{MD}})$ and the velocity $\mathbf{v}_i(t + \delta t_{\mathsf{MD}})$ depend on the initial coordinate $\mathbf{x}_i(t)$ and the velocity $\mathbf{v}_i(t)$ as well as the force $\mathbf{F}_i(\{\mathbf{x}\}(t)$ is given by

$$\begin{aligned}\mathbf{x}_i(t + \Delta t_{\mathsf{MD}}) &= \mathbf{x}_i(t) + \Delta t_{\mathsf{MD}}\mathbf{v}_i(t) + \frac{\Delta t_{\mathsf{MD}}^2}{2m_i}\mathbf{F}_i(\{\mathbf{x}\}(t)) \\ \mathbf{v}_i(t + \Delta t_{\mathsf{MD}}) &= \mathbf{v}_i(t) + \frac{\Delta t_{\mathsf{MD}}}{2}(\mathbf{F}_i(\{\mathbf{x}\}(t) + \mathbf{F}_i(\{\mathbf{x}\}(t + \Delta t_{\mathsf{MD}})).\end{aligned} \tag{2.2}$$

The weighting factors in (2.2) can be determined by Taylor expansion. The highest order derivation between the leapfrog algorithm and the exact Taylor expression is in the order of $\mathcal{O}(\Delta t_{\mathsf{MD}}^4)$. The simple computational step makes the leapfrog algorithm much more efficient than third or fourth order integrators. Combined with the robust stability for long-term simulations, the leapfrog algorithm is the preferred algorithm for microcanonical simulations in the three-dimensional highly non-equilibrium problem we face.

To artificially heat or cool the system, one must control the temperature of the system during the numerical integration step. In such a **Canonical Ensemble**, a heat exchange takes place between the system and an external heat bath. In this work, we use the Nosé-Hoover (NH) thermostat [35]. The NH thermostat adds an extra degree of freedom s to the Hamiltonian of the system. The Hamiltonian then writes

$$\begin{aligned}\mathcal{H}(\{\mathbf{x}\}, \{\mathbf{p}\}, p_s, s) &= \sum_i \frac{\mathbf{p}_i^2}{2m_i s^2} + U(\{\mathbf{x}\}) + \frac{p_s^2}{2Q} + g k_{\mathsf{B}} T \ln(s) \text{ with} \\ \mathbf{F}_i(\{\mathbf{x}\}) &= -\nabla_{\mathbf{x}_i} U(\{\mathbf{x}\}),\end{aligned} \tag{2.3}$$

where g is the number of independent momentum degrees of freedom in the system. The virtual particle interacting with the system is represented by the momentum p_s, the coordinate s, the mass Q and the temperature T. The form (2.3) results in the equations of motion

$$\frac{\mathrm{d}\mathbf{x}_i}{\mathrm{d}t} = -\frac{\mathbf{p}_i}{m_i s^2}, \tag{2.4}$$

$$\frac{\mathrm{d}\mathbf{p}_i}{\mathrm{d}t} = \mathbf{F}_i(\{\mathbf{x}\}), \tag{2.5}$$

$$\frac{\mathrm{d}s}{\mathrm{d}t} = \frac{p_s}{Q} \text{ and} \tag{2.6}$$

$$\frac{\mathrm{d}p_s}{\mathrm{d}t} = \frac{1}{s}\left(\sum_i \frac{\mathbf{p}_i^2}{m_i s^2} - g k_\mathrm{B} T\right). \tag{2.7}$$

The integration can now be done using the leapfrog algorithm (2.2). In fact, the NH thermostat describes a microcanonical system with an extended degree of freedom, which leads to similar properties compared to the microcanonical ensemble.

2.2.2 Interaction Potentials

The calculated force $\mathbf{F}_i(\{\mathbf{x}\})$ acting on the atoms includes all atomistic interactions introduced into the simulation. The choice of the underlying potential $U(\{\mathbf{x}\})$ is crucial for the result of the simulation as well as for the computational efficiency. The choice of the interaction potential depends mostly on the type of interaction that dominates in a given material. For ionic compounds, long-range interactions of the order of several lattice constants are relevant. For metals or metal compounds, short range interactions dominate due to the absence of electrostatic interactions between the atomic nuclei. In our case, the short-range interaction is modeled using the **Embedded Atom Model (EAM)**. Inside the metal, the interaction is governed by the pair interaction with the nearest neighbors as well as the interaction with the electron gas, especially the charge density inside the metal. An exemplary visualization of the pair interaction potential $\phi(r)$ as a function of the distance r between two atoms, the electron density distribution $\rho(r)$ near an atom, and the embedding energy $E_\mathrm{emb}(\rho)$ as a function of the local electron density is given in fig. 2.6. The advantage of the EAM potentials is that $\rho(r)$ and $E_\mathrm{emb}(\rho)$ fall to zero fast enough to neglect the interaction between atoms of distance $r > r_\mathrm{c}$, while the cutoff radius r_c lies between the one and the two lattice constants. In the further simulations the EAM potentials from Zope and Mishin [36] are used for the interatomic aluminum interaction.

To avoid checking all atoms in the simulation for possible interaction, cluster the simulation box into **MD Cells** with the edge width of the cutoff radius r_c, shown in fig. 2.7(a). All possible interacting atoms must now be inside the 27 neighboring cells for 3-dimensional simulations. A visualization of the interacting atoms in two dimensions is shown in fig. 2.7(b).

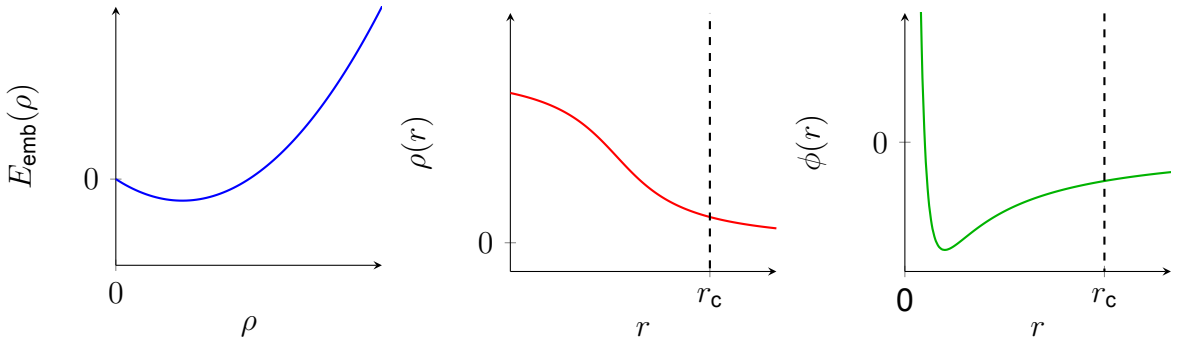

(a) Embedding Function (b) Electron Density (c) Pair Interaction

Figure 2.6: An exemplary progression of the embedding energy function (a), the electron density (b) and the pair interaction energy (c).

2.2.3 Efficiency Optimizations and Parallelization

Due to the size of the simulations, it is necessary to run the simulation in parallel on multiple CPUs. Therefore, the simulation box is divided into cuboids consisting of a 3-dimensional array of MD cells, see fig. 2.7(a). The MPI communication is used for the interaction between the boundary cells [37]. Each CPU is treated as a separate MPI threat.

For a molecular dynamics simulation with system-wide interatomic interaction, the computational time scale is of the order of $\mathcal{O}(n^2)$ for a system of n atoms. The use of the cutoff radius reduces the computation time by neglecting the interaction of atoms outside the 26 neighboring MD cells. The simulation time of the system in this case scales with $\mathcal{O}(k \cdot n)$, where the expected neighbors k are in the same MD cell and the surrounding MD cells. The expected neighbors k are related to the cutoff radius r_c, since for a simulation with uniformly distributed atoms the expected neighbors k behave linearly with the cutoff radius.

The imbalance in atom density within the sample leads to different computational loads for different CPUs. This difference in the copulation time per time step for different CPUs leads to waiting times for CPUs with lower workloads, resulting in a decrease in the efficiency of the simulation. To balance the load on the CPUs within the simulation, the boundaries of the area covered by a CPU are shifted depending on the distribution of atoms within the sample. The use of load balancing becomes more relevant for simulations on a single sphere compared to the simulation of a powder [38], due to the higher imbalance in particle density. In this case, load balancing is performed before the start of equilibration of the sample, as well as immediately after the laser penetration.

The computational effort is further reduced by changing the appropriate time step for different parts of the simulation, depending on the dynamics within the simulation. During the heating of the sample to room temperature and the equilibration of the sample before the laser interaction, timesteps up to $10\,\text{fs}$ are chosen. During laser penetration, a shorter time step in the range of $0.1\,\text{fs}$ to $1\,\text{fs}$ is required to represent the fast dynamics of the highly non-equilibrium dynamics. After the laser has left the sample and the kinetic energy is distributed in the sample, the time step can be increased step by step.

In order to avoid the displacement of atoms far outside the simulation box, periodic bound-

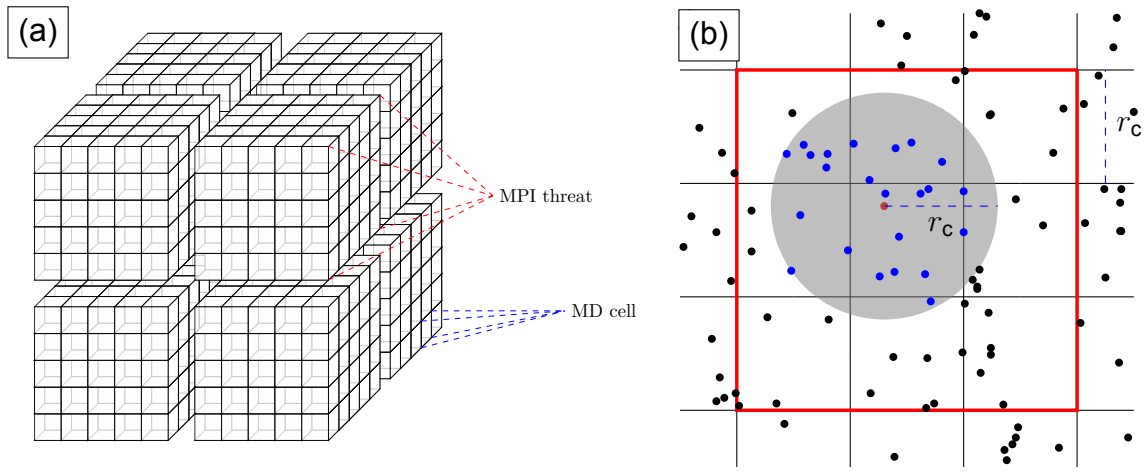

Figure 2.7: The splitting of the simulation box into MD-cells which are clustered to MPI threats is shown in (a). Illustration (b) shows the interaction atoms according to the cutoff radius r_c and the resulting relevant MD-cells for the force calculation in two dimensions.

ary conditions (PBC) combined with a filtering of atoms (see section 3.2) are used for the simulation. This limits the available positions of atoms to the size of the simulation box. Previous work has shown a huge loss in efficiency for atoms leaving the simulation box [39]. Atoms outside the simulation box lead to an imbalance in the load between CPUs, since the atoms outside the simulation box are not evenly distributed over all CPUs.

2.3 Implementation of Laser Interaction

The energy absorption process of a laser of intensity I penetrating a metallic surface is dominated by free carrier absorption (FCA). Electrons in the electron gas below the Fermi energy are excited, while as a consequence the Fermi-Dirac distribution shifts to higher electron energies, resulting in a rising electron temperature [40]. The relaxation time of the electron gas, which is synonymous with the time scale of the energy transition between them, can be derived from the Drude model. This model assumes an energy transfer between the electron gas and the atomic lattice induced by collisions of the electrons with the nuclei [41]. While the time scale of electron-phonon collisions can be determined to be approximately $8\,\mathrm{fs}$ at room temperature, it decreases exponentially at higher lattice temperatures [42]. Compared to our MD time step of the order of $1\,\mathrm{fs}$, the relaxation of the electron gas can be considered instantaneous. Consequently, it is now necessary to implement the laser absorption using a two temperature model (TTM) in the case of simulation PBF on aluminum, in contrast to the laser appellation of semiconductors [11]. The absorption of the laser energy is applied directly to the atom by rescaling its kinetic energy.

2.3.1 Lambert-Beer Law

Laser absorption in FCA is dominated by single photon absorption. This absorption mechanism can be assumed to be constant within the metal. This results in an exponential decrease of the laser intensity in the z-direction (laser direction) within the metal sample. This results in an exponentially decreasing local laser intensity.

$$I(z) = I_0 e^{-\mu z}, \tag{2.8}$$

where I_0 is the surface laser intensity and μ is the absorption coefficient, which depends on the laser frequency and the interacting material. This absorption law is known as the Lambert-Beer law [43].

For a Gaussian laser pulse in the x- and y-directions centered at x_0 and y_0, this results in a laser intensity of

$$I(x, y, z) = I_0(1 - R)e^{-\mu z} e^{-\frac{(x-x_0)^2+(y-y_0)^2}{2\sigma^2}} \tag{2.9}$$

within a massive sample. The intensity I_0 is the maximum laser intensity at the center of the laser spot, while σ describes the decrease in laser intensity in the x- and y-directions with the full width half maximum (FWHM) given by

$$\text{FWHM} = 2\sqrt{2\ln 2}\,\sigma \approx 2{,}3548\sigma. \tag{2.10}$$

The energy $\mathrm{d}E$ applied to a volume fraction $\mathrm{d}V$ per time $\mathrm{d}t$.

$$\begin{aligned} \frac{\mathrm{d}E}{\mathrm{d}V\,\mathrm{d}t} &= \mu \frac{P_{\text{tot}}}{2\pi\sigma^2} P_{\text{tot}}(1 - R)e^{-\mu z_{\text{eff}}} e^{-\frac{(x-x_0)^2+(y-y_0)^2}{2\sigma^2}}, \text{with} \\ P_{\text{tot}} &= 2\pi\sigma^2 I_0 \end{aligned} \tag{2.11}$$

is the negative derivative of (2.11) with respect to the direction of laser penetration.

2.3.2 Density Dependent Energy Absorption

To model the laser absorption as a function of the volume fraction of aluminum in an MD cell, we must somehow define an absorption coefficient μ_t of a single atom, depending on the atom type t, within a fluid or crystal. The absorption depth of $d_{\text{LB}} = 1/\mu = 80\,\text{Å}$, which corresponds to an absorption coefficient of $\mu_{\text{LB}} = 0.0125\,1/\text{Å}$, results from previous simulations of laser ablation in aluminum [44].

The laser absorption is calculated MD cell by MD cell from top to bottom. A collective absorption coefficient

$$\mu_{i_x,i_y,i_z} = \left(\sum_i \mu_{\text{type}(i)} \right) / V_{\text{cell}} \tag{2.12}$$

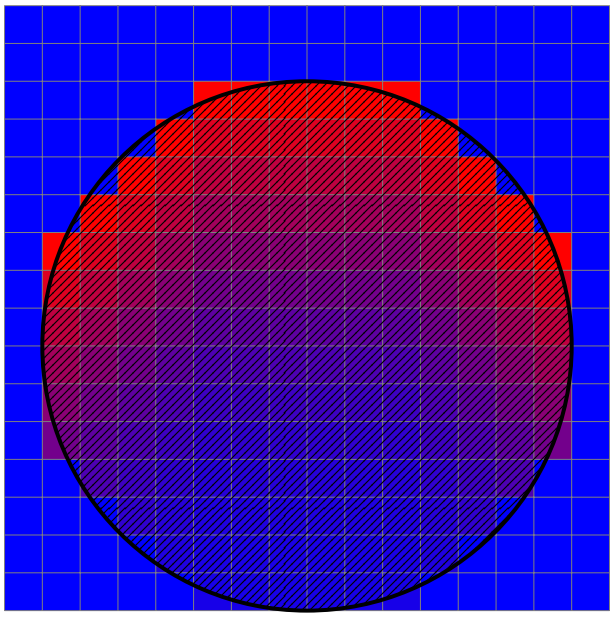

Figure 2.8: Schematic illustration of the decrease of laser intensity within a sphere, taking only MD cells including aluminum atoms into account for the absorption. More red MD cell indicate a high laser intensity as more blue illustrate a lower laser intensity. The aluminum sphere is illustrated shaded. The laser intensity is distributed uniformly in this example.

of a cell with coordinates i_x, i_y and i_z, depending on the i atoms with their animistic absorption coefficients $\mu_{\text{type}(i)}$ inside the cell of the volume V_{cell}. The cell information is then sent within the same column of cells in z-direction (same x and y coordinates).

In the solid FCC structure, an aluminum atom occupies the volume of $V_{\text{atom}} = 16.6\,\text{Å}^3$. so that the absorption coefficient can be calculated

$$\mu_{\text{atom}} = \mu V_{\text{atom}} \tag{2.13}$$

for a single atom. In the case of aluminum, the single atom absorption results in $\mu_{\text{al}} = 0.2075\,\text{Å}^2$. The local laser intensity in a cell with coordinates l_x, l_y and l_z is given by

$$I_{\text{lx,ly,lz}} = I_0 e^{-\sum_{iz>lz} \mu_{l_x,l_y,i_z} \cdot d_{cell,z}}, \tag{2.14}$$

with the length $d_{cell,z}$ of a MD cell in z-direction.

An example of the laser intensity for each MD cell within a single sphere is shown in fig. 2.8. In this case of uniform laser intensity distribution, the top MD cells at the side of the sphere receive the same laser penetration as the MD cells at the top center of the sphere. This differs from previous work that assumed an exponential decrease in laser intensity from the top of the sample regardless of the shape of the sample [45] [39].

2.4 Analyzing Tools

2.4.1 Structure Analysis

In order to analyze the lattice structure as well as the melting and recrystallizing process of the sample, we use common neighbor analysis (CNA) to differ between structure types [46]. The first step of CNA is to identify the atomic neighbors of each atom. The cutoff radius for these atoms is dependent of the crystalline structure. For an face-centered cubic (FCC) structure, this radius is located midway between first and second shell of atomic neighbors. Afterwards, pairs of atoms are classified according to their common neighbors and the underlying geometry of the common neighbors. This analysis tool allows to get information of the atomic structural behavior of defects in a recrystallized sample. Additionally, we get an insight of the equillibration time of our lattice, by tracking the time delay between laser-solid interaction and the dissolving of the lattice structure. Besides the FCC structure, the hexagonal close-packed (HCP) structure becomes relevant in the analysis of the aluminum sample, as HCP defect structure arise at recrystallization and stress application on solid aluminum.

Stress Properties

To quantify the mechanical properties of the recrystallized sample, an external stress is applied to the sample. The first method is to apply a constant stress to the sample. This is done by moving a few layers of atoms at a constant speed, while the atoms on the other side of the sample are fixed. Depending on the moving direction of the atoms, one can apply ether shear stress fig. 2.9(a) or tense and compress the sample fig. 2.9(b). Young's modulus

$$E = \frac{\sigma}{\epsilon} \tag{2.15}$$

quantifies the relationship between the external stress σ and the deformation of the specimen quantified by the axial strain ϵ [47]. While the external stress $\sigma = \mathrm{F}/\mathrm{A}$ results from the normal force on the continuous moving layer and the axial strain ϵ results from the relative change in length of the specimen.

The second method of obtaining mechanical properties of the sample is to apply shock waves to the sample. In this case, a fracture of atoms is set to an initial velocity $\mathbf{v}_i$. This external momentum applied to the sample creates a shock wave that travels through the sample. The velocity and scattering of the shock wave inside the sample can be compared between samples and in different directions.

The stress simulations are performed on fully recrystallized samples at room temperature, on sections of the simulated sample.

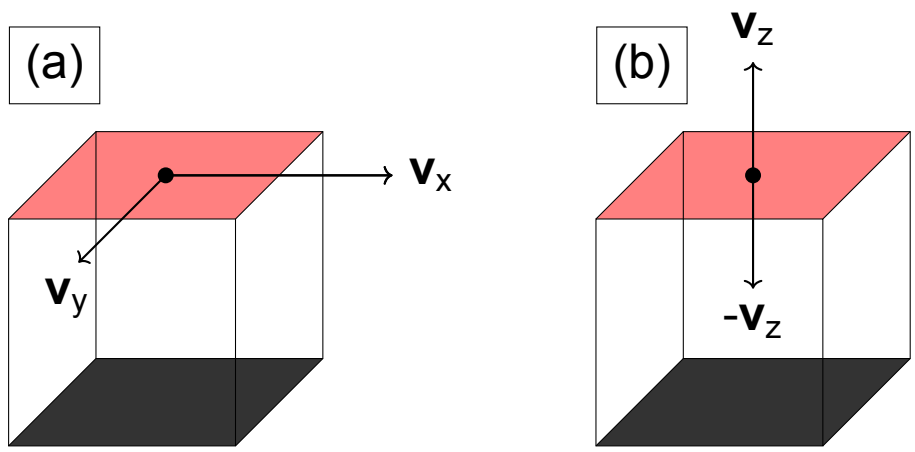

Figure 2.9: Illustration of the application of shear stress (a) and compression/tension (b) on a sample. The black ground is fixed, while the red fraction is moved into a certain direction with the velocity $\mathbf{v}_i$.

2.4.2 Energy Analysis

In addition to the mechanical and structural properties of the sample, MD simulations provide insight into the atomistic behavior during the laser interaction. Depending on the laser parameters, the evaporated energy as well as the material loss during the simulation are extracted from the simulation. Therefore, not only the energy E_{Laser} applied to the sample via the energy resealing of the atoms is tracked, but also the energy of the atoms leaving the simulation box at the top is calculated and added.

Since the simulation box is periodic in the x-direction and in the y-direction during laser penetration, aluminum atoms that cross the boundaries of the simulation cell in the z-direction are removed from the simulation along with their kinetic energy. These removed energies E_{diss} are summed to obtain an effective energy.

$$E_{\text{eff}} = E_{\text{laser}} - E_{\text{diss}}. \tag{2.16}$$

In addition to the energy applied to the sample and the energy leaving the simulation box, the temperature of the entire sample and the kinetic energy of each atom within the simulation can be calculated within the MD simulation. Additionally, the potential energy within the sample can be calculated.

Chapter 3

Simulation Setup and Parametrization

In this chapter, the validation of the applied energy by the laser module (section 3.1.1, the size limitations in relation to finite size effects (section 3.1.2) is mentioned based on single sphere simulations. Some specific characteristics like the removing of atoms (section 3.2, the gas density (section 3.3 and the specific gravity within the simulation (section 3.4) are explained. Also the creation of the powder sample (section 2.1.4) and the calibration as well as the heating to room temperature is explained (section 3.6). The modeling of the stress tests on the crystallized samples is discussed in section 3.7.

3.1 Single Sphere Simulations

3.1.1 Laser Module Energy Validation

Single sphere simulations are used to validate the energy applied to the sample by the laser module. The interaction between the laser and the metal sample is modeled as described in section 2.3. In this implementation, the energy applied to the sample is tracked as the laser penetrates the sample. The laser energy applied to the sample in the simulation can be compared to the analytical result. The simulation is performed on a sphere with radius 500 Å and laser power 2500 eV$/10$ 18fs, laser FWHM 250 Å and laser velocity 10.18 fs. To show the density dependent absorption, an extra small penetration depth of 1 Å is chosen. The simulation adds up the total energy for one time step, which allows the calculation of the actual laser power added to the sample. The atomic shape as well as the distribution of aluminum atoms in the x-direction is shown in fig. 3.1. As the laser passes the sample, the upper layers of the aluminum sphere evaporate due to the short penetration depth. After the laser passes the sample, some vaporized aluminum surrounds the sphere as the upper layers of the sphere melt.

For the analytical result, the applied energy eq. (2.11) is integrated over the volume of the sphere. The position x_0 is replaced by vt and by integration over the volume the actual laser power can be determined. The solutions of the integral P_{th} as well as the power during the simulation P_{sim} are shown in fig. 3.2 for two different laser energies. The results of the

integral are calculated numerically using the Python package SciPy [48].

For the laser power of $P = 80\,\mathrm{eV}/10.18\mathrm{fs}$, the results from the integral and the power in the simulation show good agreement, see fig. 3.2(b). At this small power, the sample has been heated, but there is no evaporation or deformation of the sphere. The difference between the width of the absorption profile and the maximum power is due to the absorption per MD cell. The finite size of an MD cell leads to a deviation from the continuous absorption assumed in the integral.

The simulation at a laser power of $P = 1280\,\mathrm{eV}/10.18\mathrm{fs}$ leads to a larger deviation from the power calculated in the integral. The reason for the difference in shape is the deformation of the sphere and the interaction with the vaporized aluminum. The distribution of aluminum atoms in fig. 3.1 shows the amount of vaporized aluminum evenly distributed in the z-direction within the sample. When the laser reaches the part of the sample to the right of the sphere, vaporized aluminum has already entered this part of the simulation box. This leads to a shoulder in the absorption profile in fig. 3.2(b).

In general, the power in the simulation is in good agreement with the solution of the integral. The deviation is not relevant for the dynamics of the sample. Especially for larger penetration depths, the finite size effect of the MD cells becomes less relevant due to a flatter absorption in the z-direction.

3.1.2 Finite Size Effects

To get a first impression of the melting process and the general dynamics of the simulation, melting processes are performed on a single sphere. Figure 3.3 shows the laser penetration of a single sphere with radius $50\,\text{Å}$. The finite size effect already mentioned for the SLS simulation causes a deformation of the sphere at room temperature, as shown in fig. 3.3(b). The images 3.3(c) and 3.3(d) model the laser interaction with the sphere, while the deformation of the sphere caused by the laser occurs with a time delay after the laser has passed the sample.

For laser ablation in this sample size, the formation of droplets in the ablated material can be observed due to surface tension. In addition to the deformation of the area adjacent to the bottom, spheres of this size behave similarly to larger spheres, as shown in fig. 3.1. For further tests, powder particles down to the radius of $50\,\text{Å}$ will be used, as finite size effects already affect the simulation of such small spheres at finite temperatures. For laser ablation, however, the overall behavior is mostly similar to that of larger spheres.

3.2 Removing Atoms

Since PBC is used in the x- and y-directions of the sample, aluminum atoms leaving the simulation box in the z-direction are removed from the sample. Since the PBF process sprays metal liquid all over the experiment, this material does not contribute to the resulting

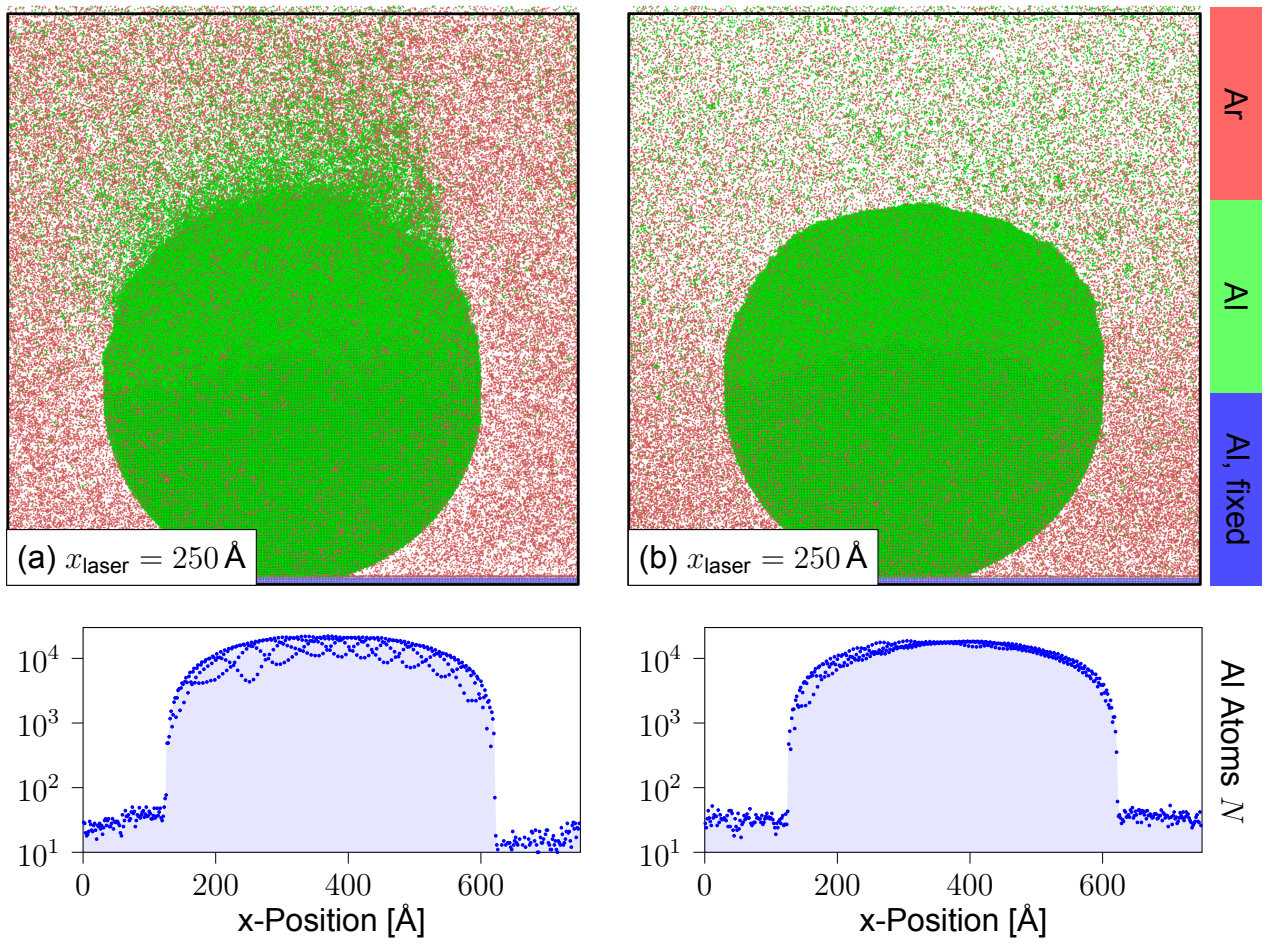

Figure 3.1: The dynamics of a single sphere during laser penetration is illustrated. Figure (a) shows the sphere and the distribution of aluminum at a laser position of $250\,\text{Å}$. Figure (b) shows the sphere and the distribution of aluminum at a laser position of $750\,\text{Å}$.

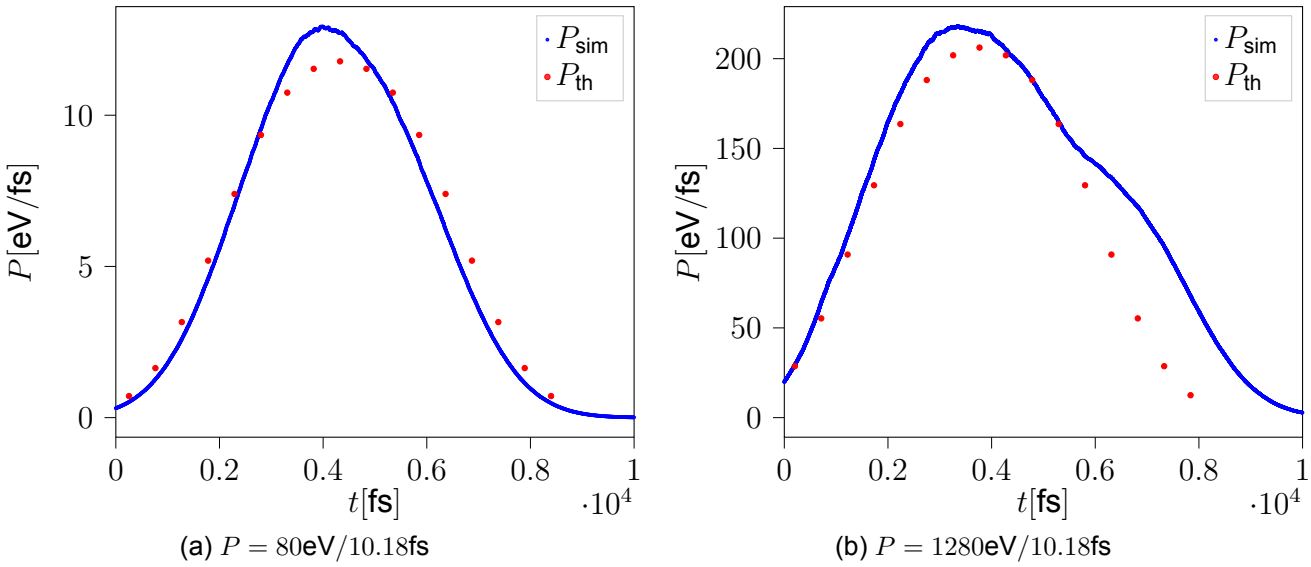

Figure 3.2: The added kinetic energy in the simulation P_{sim} is shown with the integral of (2.11) over the sphere.

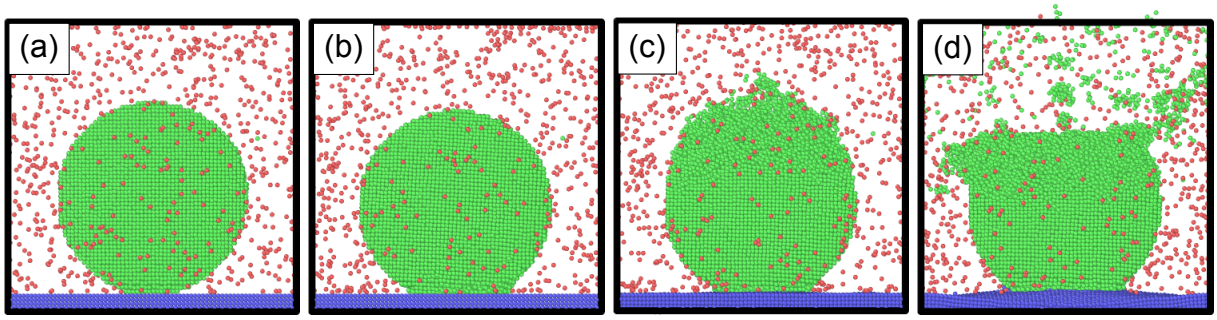

Figure 3.3: Laser ablation on a sphere of radius 50 Å. (a) shows the initial powder sample before equilibration. (b) shows the equilibrated sphere. (c) shows the melting process immediately after the laser leaves the sample. (d) shows the explosion of the sample 150 ps after the laser has left the sample.

sample and its exact motion is not of interest for the simulation. The filter module works by removing atoms in an optional layer above the sample from the simulation. To quantify the loss of material and energy caused by the removed atoms, the kinetic energy of the removed atoms as well as the total number of atoms in the sample is tracked for each time step. In comparison to the metal atoms, the gas atoms are reflected at the upper boundary of the simulation box to ensure a constant gas density within the sample, as the gas would quickly soak out of the simulation box due to its highly diffusive behavior.

3.3 Gas Environment

A protection gas is added to the sample in order to model defects like gas pockets. For a simulation in vacuum, voids within the sample can just collapse within the liquid metal phase. The gas density is chosen to model a gas continuum, which results in more then ten times atmosphere gas density. In order to not distort the overall dynamics by the increased gas density, the gas interaction strength is adapted to the gas density. For simulations without PBC or an applied filter an the aluminum, the gas needs a different treatment. In the absence of PBC, the diffusion of the gas far out of the simulation box leads to an immense decrease in computational efficiency. For simulations including a filter, the gas would be sucked out of the simulation due to its high mobility. In order to keep the gas density constant over the simulation, the surrounding gas somehow needs to be reflected. Therefore, the z-component of the gas atoms is turned when the gas atoms leave the simulation box on the top. This leads to a constant equal gas distribution during the laser interaction, see fig. 4.3. The limitations of this simple model occur when the temperature is lowered, as seen in fig. 4.11. For lower temperatures, gas is trapped of top of the sample, which leads to a lowering of gas density in the rest of the sample. While this effect generally is to avoid, for this application the restrictions are negligible, because the main impact on the cooling arises from gas trapped inside the sample. For further applications, one could implement the surrounding gas using a grand-canonical ensemble with a gas reservoir [49].

3.4 Gravity

After the laser penetration of the sample and the associated speed of rewelding, the liquid metal is injected equally in all directions. To achieve the formation of a melt on the bottom, the effect of gravity plays a big role. Even for PBF in the size range of μm, rates in the order of $10^4 - 10^5$K/s are experimentally determined [50]. This leads to a lifetime of the melt pool in the range of several milliseconds [51]. In comparison, MD simulations provide a timescale in the picosecond range in the context of a typical timestep on the order of a femtosecond. In order for droplets and fountains to settle on the bottom of the sample, gravity must be increased by several factors. The fall distance

$$\Delta z = -\frac{1}{2} g_{\text{mod}} t_{\text{MD}}^2 \tag{3.1}$$

is given by the modified gravity g_{mod} and the simulated time t_{MD}. For the Earth's gravity of $g_{\text{Earth}} = 9.81\,\text{m/s}^2 = 9.81 \cdot 10^{-14}\,\text{Å/ps}^2$ results in a fall distance of $\Delta z = 4.9 \cdot 10^{-10}$ Å for a simulation time of $t_{\text{MD}} = 100$ ps. To observe the falling of droplets in a sample with a total size in of 100-1000 Å, the gravitational pull on the atoms is given by $g_{\text{mod}} = 10^{11} g_{\text{earth}}$.

3.5 Powder Samples

The goal of creating powder samples is to replicate experimental powder samples, despite the size limitations of the simulation. The finest manufactured powders can reach a grain size down to less then 100 nm [52]. Because such fine grains require several hours of grinding, the finest powders used for PBF have grain sizes down to $20\,\mu m$ [29]. In order to create a powder for simulation, the computational effort must be weighed against the desired results of the simulation. To analyze energetic structural defects at the lattice scale and evaporation at the atomistic scale, one does not automatically need to push the limits of computational resources, but rather run several smaller simulations and analyze the dependencies of the input parameters and the resulting sample. On the other hand, one must choose a sample size large enough to observe dynamics comparable to experimental observations and not dominated by the finite size effect, see fig. 3.3. To run the final simulation on 32 nodes, with 4096 MPI threats and a load of about 2000 atoms per CPU, the total sample size should be in the range of $1 \cdot 10^7$ atoms. To create a powder of this size, a box size of 1000x400x800 Å is used. Since the laser moves in the x-direction, the choice of a reduction of the simulation cell in the y-direction comes from the interest in the dynamics in the z-direction, see section 2.4.

The pattern for a PBF simulation is created in three main steps. First, the geometry of the powder configuration is created. In this step, the width of the base, the position and radius of each grain ball, and the size of the simulation box are defined. In our case the powder is modeled with a size distribution consisting of two Gaussian peaks, see fig. 2.3. The powder

Table 3.1: Particle properties of of the powder samples. The mean values of fine and coarse particles are given by μ_{fine} and μ_{coarse}, as the associated variance is given by $\mu_{\text{coarse}}/$ and $\sigma_{\text{fine}}/$. The volume fraction of coarse particles ϕ_{coarse} and the total powder volume fraction ϕ_{tot} lead to the total atom number N_{tot}.

sample name	μ_{fine}/Å	μ_{coarse}/Å	σ_{fine}/Å	σ_{coarse}/Å	ϕ_{coarse}	ϕ_{tot}	N_{tot}
coarse015	50	200	10	50	0.15	0.30	10066459
coarse02	50	200	10	50	0.2	0.31	10397100
coarse025	50	200	10	50	0.25	0.32	11129182
coarse00	50	200	10	50	0	0.28	9249713

configuration is then defined by the mean size μ_{fine} and the variance σ_{fine} of the fines, the mean size μ_{coarse} and the variance σ_{fine} of the coarse particles, as the volume fraction ϕ_{coarse} for the coarse particles, and the total powder volume fraction ϕ_{tot}. To achieve this, coarse particles are picked from the underlying Gaussian distribution and placed at a random position in the simulation box. If the particle overlaps with a previous particle, the bottom or the top of the simulation box, a new random position is chosen. For a position with no overlap, the particle is placed there and a new particle is picked from the size distribution. After a certain number of steps without finding an empty space, a new particle is selected without placing the current one. When the density fraction ϕ_{coarse} is reached, the fine particles are placed in the same way until the total density fraction ϕ_{tot} is reached. For geometric reasons, the maximum powder density fraction ϕ_{tot} also depends on the powder size distribution. This effect plays a minor role for PDF, since the packaging of experimental powders is much looser than this limit.

In order not to have a dynamic dominated by finite size effects, μ_{fine} is chosen as in the simulation in fig. 3.3, where finite size effects occur, but the overall dynamics is not dominated by them. The mean value of μ_{coarse} is defined in half of the simulation box in y-direction, in order to keep the properties of a powder also for the coarse particles. The selected powder parameters are listed in table 3.1.

In the second step, the spheres and the bottom are filled with the FCC structure of aluminum, and the empty space is filled with randomly distributed argon atoms. The orientation of the FCC lattice is randomly rotated for each individual sphere. The resulting total number N_{tot} of atoms per sample is listed in table 3.1.

3.6 Sample Equilibration

Before starting the actual PDF simulation, the sample must be in thermal equilibrium. Therefore, an NH thermostat is used. Due to the presence of gas surrounding the aluminum spheres, the ideal selection of the virtual mass Q interacting with the system is different for the gas and the aluminum spheres. It is emphasized that the selection applied to the aluminum spheres gives sufficient results, while the equilibration of the aluminum mass takes the longest time anyway. In order to heat the surrounding gas in the sample, it is necessary

to increase the MD timestep starting from 0.01 fs to avoid that gas atoms crash into the lattice structure of the aluminum spheres and cause a huge increase of the local kinetic energy. The time step can be increased up to 1 fs where at least 200000 MD steps are performed to speed up the equilibration process. Before starting the PBF simulation, some steps are performed in the microcanonical ensemble, since the PBF simulation is also performed in the microcanonical ensemble. In addition to equillibration, gravity acts on the spheres, causing the larger spheres to condense at the bottom. An example for the sample equilibration is given in section 5.3

3.7 Deformation Stress

To apply deformation stress to the recrystallized sample, the simulation box is cut in z-direction (fig. 3.4(a)) to increase the computational efficiency, while the surrounding gas above the aluminum sample does not affect the results of the simulation. The *IMD* provides several deformation methods to compress, tense, or apply a shear stress to the sample. To induce the deformation of the sample, simply apply a translation

$$\mathbf{x}' = \mathbf{x} + s\mathbf{n} \tag{3.2}$$

on an atom with position $\mathbf{x}$. The new position $\mathbf{x}'$ differs from the previous position by the magnitude s and the direction $\mathbf{n}$. This transition takes place within the MD step, after the momentum and position have been updated according to the used integrator, see section 2.2.1. The translation is applied only to the atoms of a certain virtual type. Therefore, the upper aluminum layers, including the upper 30 Å of the sample, are assigned to an extra virtual atom type in order to apply the translation (3.2) exclusively to these atoms. The bottom of the sample is still fixed, using another virtual atom type. To compare the results of the samples with gas pockets, a sample from a simulation without surrounding gas is approached, see fig. 3.4(b). The stress applied to the specimen is extracted from the force on the moving virtual type atoms in the direction of motion.

Another problem arises from the interaction of the different virtual types. If we look at the compression of a sample, a constant translation on the upper particles leads to an increasing force from the sample below to the virtual type atoms above. This results in a non-linear compression of the sample, as well as a maximum compression depending on the external translation, while the sample heats up due to the external impact. This leads to a hot fluid pressing on the sample as shown in fig. 3.4(c). To avoid this behavior, limit the interaction between the virtual type atoms and the sample underneath in the translation direction. For compression or tension, the virtual type atoms are still able to form structures with the neighboring atoms, but a linear motion in z-direction is ensured in these cases.

Deformation processes, unlike laser interaction, typically take place in thermal equilibrium. Consequently, after each translation (3.2), the system must equilibrate for a certain

number of time steps depending on the size of the translation. Very large translation steps or an insufficient number of timesteps between the transition steps lead to a non-physical behavior as in fig. 3.4(d). In this case of stress applied to the specimen, the specimen fails directly at the boundary between the different virtual types and not at the weakest part of the specimen. However, in the MD simulation, applying stress within thermal equilibrium introduces other problems into the simulation. First, the time scale limits the strain rate to achieve a strain of 20% of the sample size. The strain rate in the MD simulations is on the order of $10^8 - 10^{10}\,1/\mathrm{s}$, while the strain in the experiment is on the order of $10^{-2} - 10^4\,1/\mathrm{s}$ [53]. Despite limitations in simulation time, the calculated stress can hardly be extracted from fluctuation due to the small size of the sample.

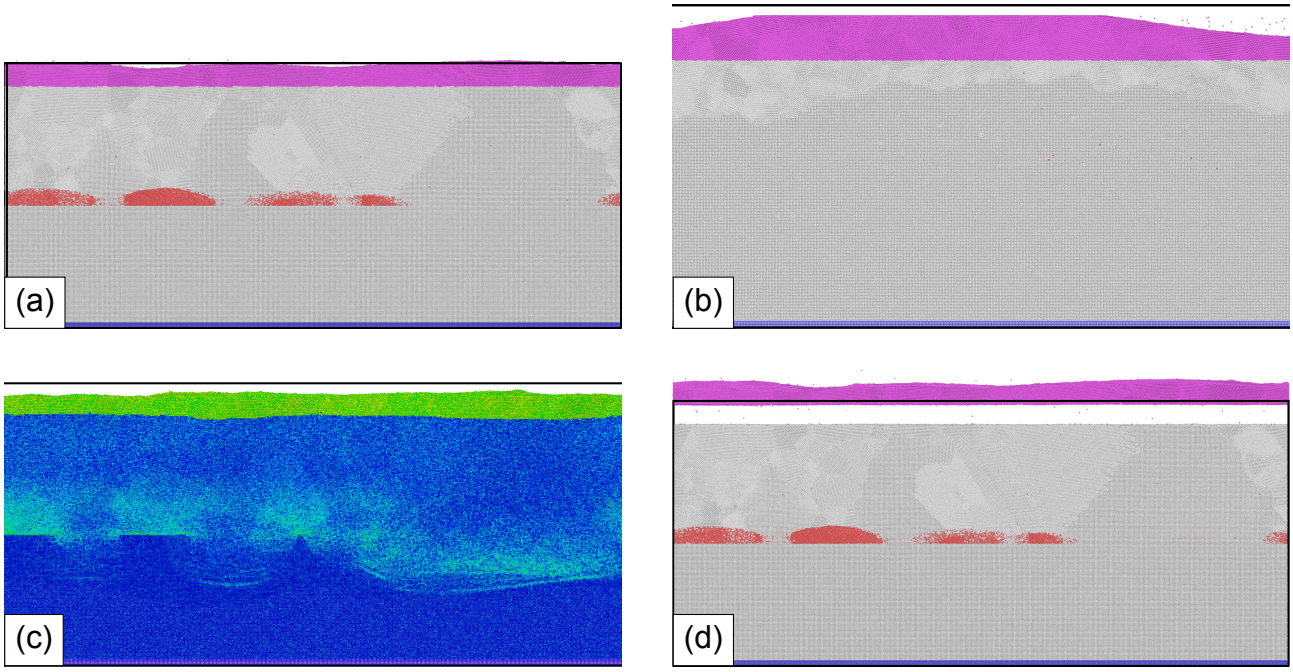

Figure 3.4: The figures (a) and (b) show the samples, which are used for the stress resistance test with and without surrounding gas. The blue base layer is fixed in all three directions, while the pink upper layer is moved in order to apply stress to the sample. Figure (c) shows the heating of the sample for fast compression, while figure (d) shows the breaking out of equilibrium of the upper layer from the rest of the sample for fast tension.

Chapter 4

Simulation Results

4.1 Melting Dynamics

In order to understand the formation of defects and porosity within the produced sample, the simulation approach provides insights into the melting process, which are not accessible in an experimental setup. This section describes the melting dynamics for different laser parameters and powder configurations are described.

First, to compare different laser parameters, we use the same powder configuration for different simulations with varying laser parameters. The chosen powder configuration *coarse02* for this step contains a volume fraction of 0.2 coarse particles, see table 3.1. Due to the high computational effort for each simulation, a hole matrix of parameters is not tested, but the evolution of simulation in the context of a change in laser scanning speed and laser power is simulated, see fig. 4.1. The choice of the parameters is derived from section 3.1.1.

The dynamics of the melting and evaporation behavior as a function of the laser velocity is discussed in detail using the simulations with the laser power $P_{\text{Laser}} = 2500\,\text{eV}/10\,18\text{fs}$ and velocity $v_{\text{Laser}} = 1.0\,\text{Å}/10\,18\text{fs}$ as well as $P_{\text{Laser}} = 2000\,\text{eV}/10\,18\text{fs}$ and $v_{\text{Laser}} = 0.5\,\text{Å}/10\,18\text{fs}$. For all further simulations the laser is turned on with the center of the laser beam at $\mathbf{x}_{\text{laser on}} = -100\,\text{Å}$ ($-100\,\text{Å}$ left of the simulation box) and moving in positive x-directions. The laser will turn off after passing the center of the laser beam $\mathbf{x}_{\text{laser on}} = 100\,\text{Å}$ ($-100\,\text{Å}$ to the right of the simulation box). The center of the laser beam is always centered in y-direction with respect to the simulation box, see fig. 4.2.

The melting process for laser power $P_{\text{Laser}} = 2500\,\text{eV}/10\,18\text{fs}$ and velocity $v_{\text{Laser}} = 1.0\,\text{Å}/10\,18\text{fs}$ is shown in fig. 4.3. The melting and evaporation process during and after laser penetration is shown in fig. 4.3. The time t_1 is the time after the laser has been turned off.

The fig. 4.3 shows the kinetic energy of the atoms in the sample for different times of the simulation, using the parameters $P_{\text{Laser}} = 2500\,\text{eV}/10.18\text{fs}$ and $v_{\text{Laser}} = 1.0\,\text{Å}/10.18\text{fs}$. The laser is switched off at $t = 12.216\,\text{ps}$ after the sample has passed. At time $t = 10.18\,\text{fs}$ the laser is on the right side of the sample and has almost passed the sample. The penetration

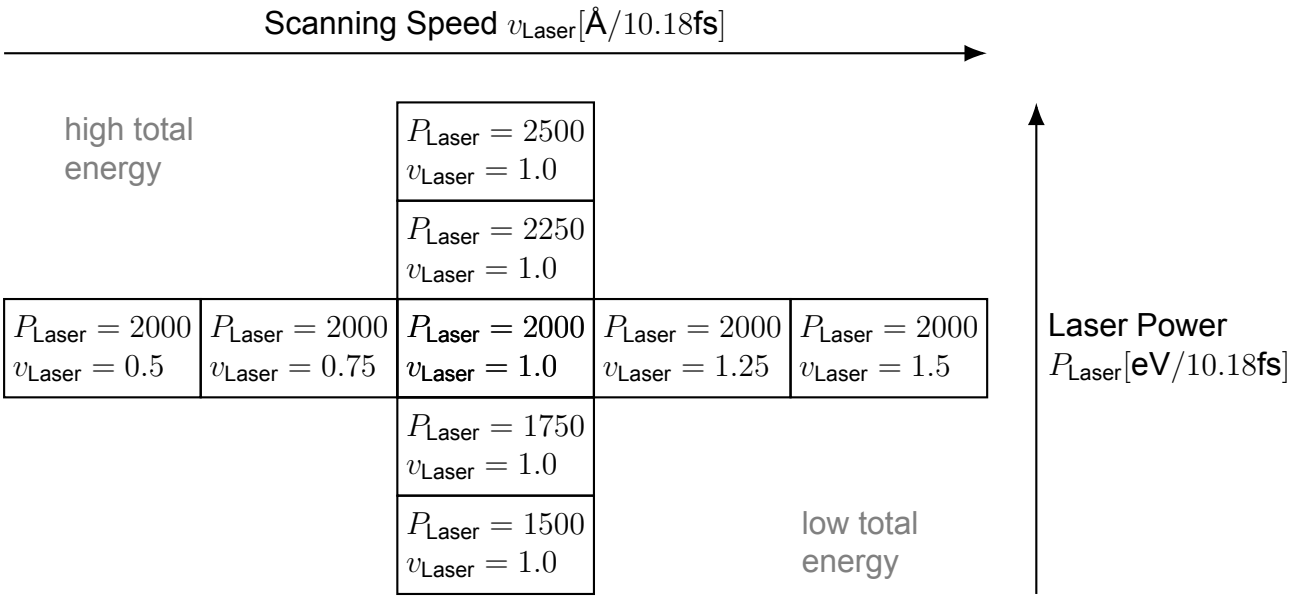

Figure 4.1: Visualization of simulated laser parameters.

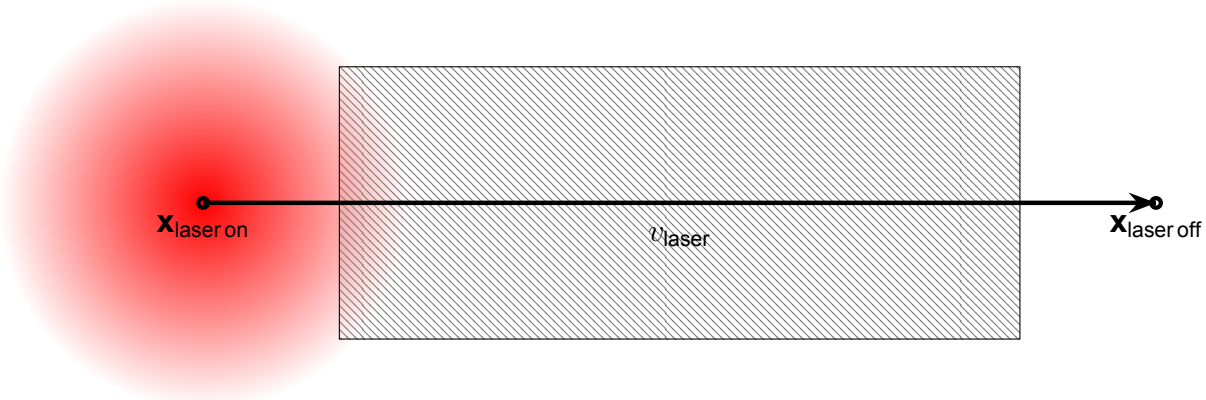

Figure 4.2: Illustration of the laser movement over the sample in x-direction from with the velocity v_{laser}. The laser is turned on at $\mathbf{x}_{\text{laser on}}$ and turned of at $\mathbf{x}_{\text{laser of}}$.

of the laser causes an increase in the kinetic energy of the atoms on top of the sample with a decrease in the z-direction. After the laser has left the sample, temperatures well above the melting temperature of $k_\mathrm{b}T_\mathrm{m} = 0.08\,\mathrm{eV}$ and the boiling temperature of $k_\mathrm{b}T_\mathrm{b} = 0.21\,\mathrm{eV}$ are locally reached at the top of the sample.

The energy transfer takes place by radiation of the laser energy within the sample. Depending on the powder structure, the laser directly penetrates the lower regions of the powder and the bottom. On the right side of the sample, the powder begins to evaporate, while in the center of the sample, despite the increase in kinetic energy, the structure has not yet fundamentally broken. This delay between the laser interaction and the melting of the sample is in agreement with the theoretical results of the Drude model of aluminum [54].

At time $t_1 = 12.725\,\mathrm{fs}$ after the laser has passed, the upper part of the sample has mostly melted and evaporated, while several fountains of liquid aluminum can be observed. In the lower parts of the sample, heat conduction causes a more uniform distribution of the kinetic within the sample. In this step one can also observe an immense heating of the surrounding gas. Collisions between vaporized aluminum atoms with high kinetic energy cause the heating. The low interaction of the surrounding gas with the colder aluminum sample and the reflection of gas atoms at the top of the simulation box lead to a gas temperature above the aluminum temperature despite the lack of interaction between the surrounding gas and the laser.

At time $t_1 = 38.175\,\mathrm{fs}$ the influence of gravity becomes visible as the molten aluminum begins to solidify. The surface tension causes smaller fountains to coalesce into larger ones. By lowering the molten aluminum, more powder particles melt until the melt fuses to the bottom shown for time $t_1 = 279.95\,\mathrm{fs}$. The temperature within the melt equilibrates and evolves to a temperature above the melting point and below the boiling point.

Figure 4.4 shows the kinetic energy of the atoms in the sample for different times of the simulation using the parameters $P_\mathrm{Laser} = 2000\,\mathrm{eV}/10\,18\mathrm{ps}$ and velocity $v_\mathrm{Laser} = 0.5\,\text{Å}/10\,18\mathrm{fs}$. The laser is turned off at $t = 24.432\,\mathrm{ps}$ after passing the sample. At time $t = 10.18\,\mathrm{ps}$, the explosion of the sample can be seen on the left side, while the laser has not even reached the center of the sample. In fig. 4.3(a), one can also observe the influence of the PBC in the x-direction from the heating of the sample on its right side. Temperatures above the boiling point are reached at the point of laser penetration.

After the laser is turned off at time $t_1 = 0\,\mathrm{ps}$, the surface of the sample is completely molten or vaporized, while fountains and droplets have formed above the sample. While the fountains melt for $t_1 = 10.18\,\mathrm{ps}$ and $t_1 = 30.54\,\mathrm{ps}$.

Figure 4.5 shows the kinetic energy of the atoms in the sample for different times of the simulation using the parameters $P_\mathrm{Laser} = 2000\,\mathrm{eV}/10\,18\mathrm{ps}$ and velocity $v_\mathrm{Laser} = 1.5\,\text{Å}/10\,18\mathrm{fs}$. In the upper part of the sample, the powder particles begin to melt as the temperature reaches above the melting point, while the temperature does not exceed the boiling point. Compared

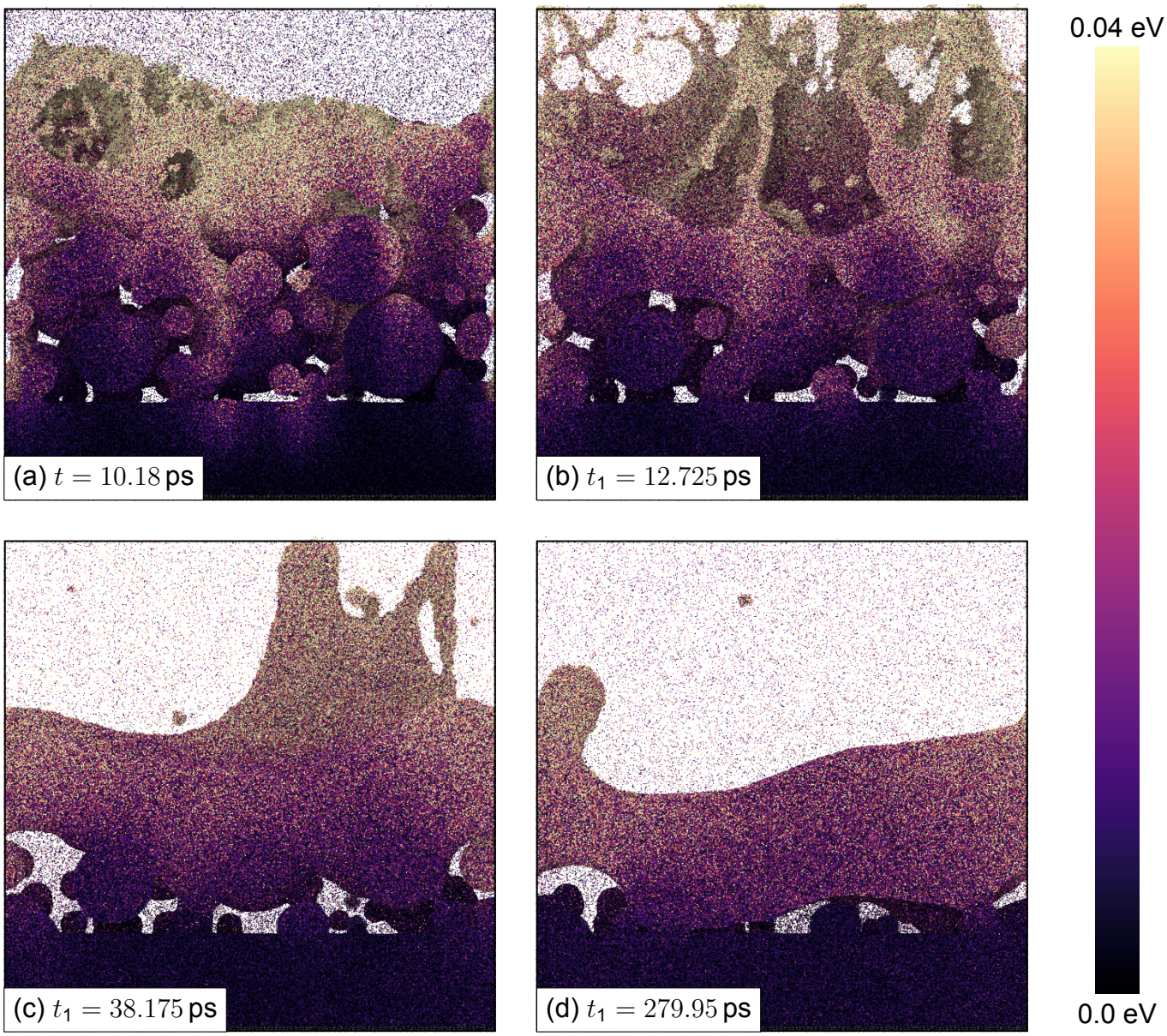

Figure 4.3: The heat distribution within the sample *coarse02* for laser parameters $P_{\text{Peak}} = 2500\,\text{eV}/10\,18\text{fs}$ and $v = 1.0\,\text{Å}/10\,18\text{fs}$. The time t gives the total simulation time while the time t_1 describes the time, which passed after the laser left the sample. The kinetic energy of each atom is given by the color.

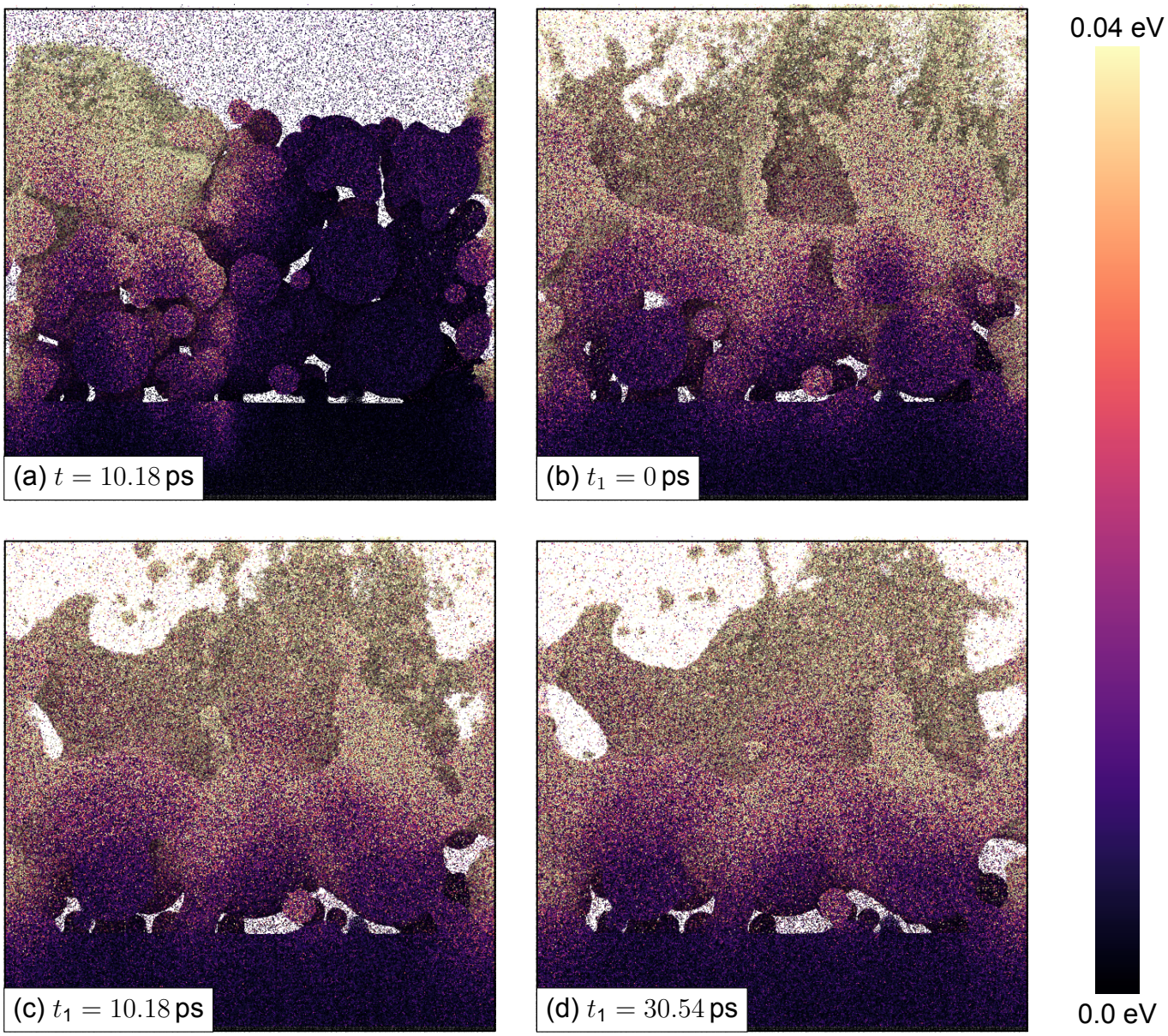

Figure 4.4: The heat distribution within the sample *coarse02* for laser parameters $P_{\text{Peak}} = 2000\text{eV}/10.18\text{fs}$ and $v = 0.5\text{Å}/10.18\text{fs}$. The time t gives the total simulation time while the time t_1 describes the time, which passed after the laser left the sample. The kinetic energy of each atom is given by the color.

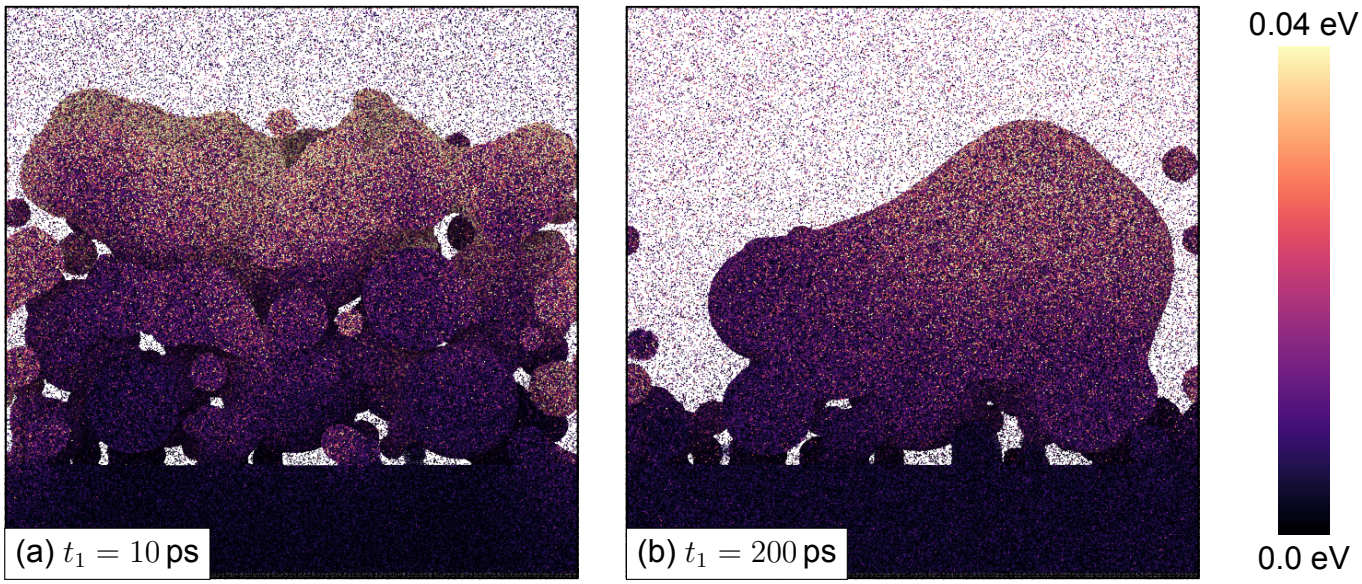

Figure 4.5: The heat distribution within the sample *coarse02* for laser parameters $P_{\text{Peak}} = 2000\text{eV}/10.18\text{fs}$ and $v = 1.5\text{Å}/10.18\text{fs}$. The time t_1 describes the time, which passed after the laser left the sample. The kinetic energy of each atom is given by the color.

to laser penetration with higher laser energy as shown in figures 4.4 and 4.3, no fountains or droplets are formed at temperatures far above the boiling point.

At the time $t_1 = 200\,\text{ps}$, heat diffusion leads to more melting. The bottom powder particles in this simulation remain unaffected by the laser penetration due to the low total energy applied.

In comparison, the surrounding gas in this simulation is heated less at low laser energy than at high laser energy. A possible explanation is the lower peak power of the interaction laser, which results in a lower maximum kinetic energy of the aluminum atom despite the slightly higher total applied energy.

While the energy transfer to the lower parts of the sample was dominated by conduction at higher energy and higher scan speed, the simulation at lower power and lower scan speed shows a greater influence of convective energy distribution. This is due to the different melting dynamics caused by the relaxation time of the aluminum powder. At a high scan speed, the powder remains largely unchanged as the laser scans the sample, while afterwards the dynamics are governed by the energy applied to the atoms by the laser. In contrast, at a slower scan speed, the melting process begins while the laser is still penetrating the molten atoms. This interaction between the molten atoms with high mobility leads to a change in the dynamics of the PBF process. One consequence is a higher conductive energy distribution, resulting in faster melting of lower parts of the sample. The higher mobility at a lower temperature prevents complete vaporization of the aluminum powder and favors droplet formation.

At higher laser velocity and lower laser power, resulting in lower total energy input, no fountains or droplets are formed because the temperature does not exceed the boiling temperature of aluminum. At lower energy input, no effects of laser ablation can be seen, while

the powder is heated above the malting point, leading to fusion of particles in the upper part of the sample driven by surface tension.

4.1.1 Powder Sample Energy Properties

To get a deeper insight into the dynamics of the melting process, in this section we take a closer look at the temperature evolution of the sample during the laser interaction, as well as the absorbed energy and the energy leaving the simulation box due to vaporization of aluminum. The increase of the average temperature within the sample is shown in fig. 4.6 (a) for a varying laser velocity and in fig. 4.6 (b) for a varying laser power at constant laser velocity. The figures 4.6 (c) and (d) show the corresponding evaporated energy. As expected, the sample temperature increases as the laser penetrates the sample. The temperature rise shows a linear behavior while the distance between the center of the laser spot and the edge of the sample in the x-direction is greater than the FWHM of the laser spot. As the laser enters and leaves the sample, the temperature rise of the sample is flat due to the Gaussian shape of the laser spot. The decrease in temperature after the laser leaves the sample can be explained by evaporated energy. The figures 4.6(c) and (d) show that, with one exception, evaporation starts after the laser has left the sample. As mentioned in section 4.1, for a slow laser speed compared to the phonon relaxation time, the dynamics of the system changes, leading to a higher amount of vaporized energy during laser penetration. This leads to a temperature decrease even before the laser has completely left the sample, see fig. 4.6 (a). In all simulations, the amount of vaporized energy is consistent with the temperature decrease in the sample, further validating the simulation framework.

Figure 4.7 shows the total energy E_{tot} applied to the sample as well as the effective energy E_{eff} excluding the evaporated energy. For varying laser velocity and laser power, the total absorbed energy E_{tot} agrees with the theoretical value of the absorbed energy for the total absorption of laser energy within the simulation box. This behavior is due to the sample depth being much larger than the absorption coefficient. Absorption values slightly larger than the theoretical total absorption are due to the modeling of the absorption, see section 2.3.2. The difference between the theoretical added energy and the energy added in the simulation is discussed in detail in section 3.1.1. This error does not affect the further results of this paper. The effective heat E_{eff}, which is relevant for the melting of the sample, deviates from the total energy E_{tot} with increasing laser power and decreasing laser velocity. The vaporized energy E_{diss} in relation to the total energy E_{tot} is shown in fig. 4.8(a) the vaporized energy is negligible.

This leads us to the ablation threshold energy in the powder sample of $E_{\text{th}} = 2 \cdot 10^6\,\text{eV}$. Considering the penetration area of $A = 1000\,\text{Å} \cdot 400\,\text{Å} = 4 \cdot 10^5\,\text{Å}^2$ from the direction of the laser, the ablation threshold is $I_{\text{th}} = 5\,\text{eV}/\text{Å}^2$. Above this threshold, the vaporized energy increases as the total laser energy increases. The increase tends to be mostly linear, as the

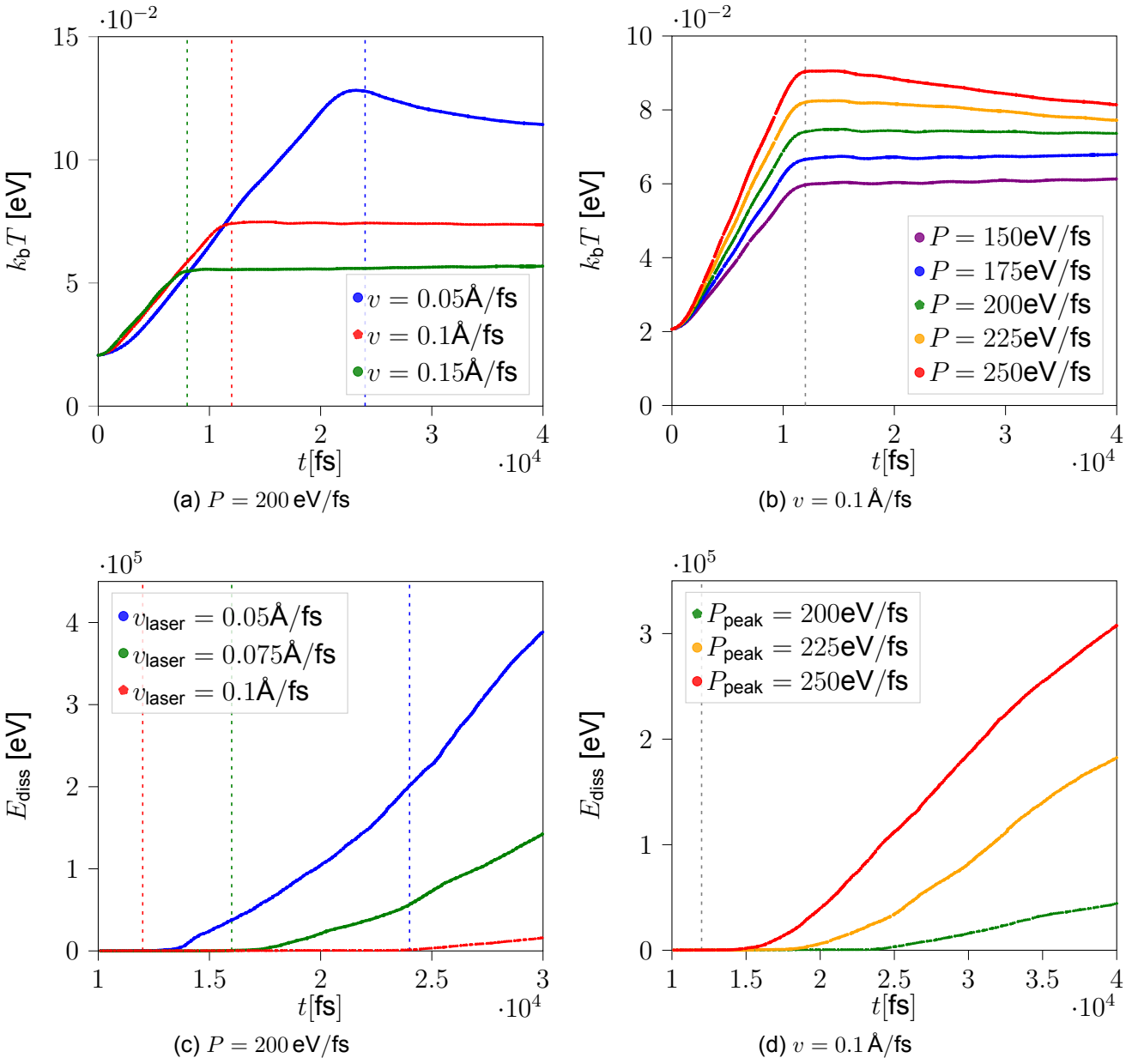

Figure 4.6: The figures (a) and (b) show the increase of temperature of the sample for different laser parameters. The Figure(c) and (d) show the disappeared energy, whereas the dotted lines mark the time, the laser is turned of.

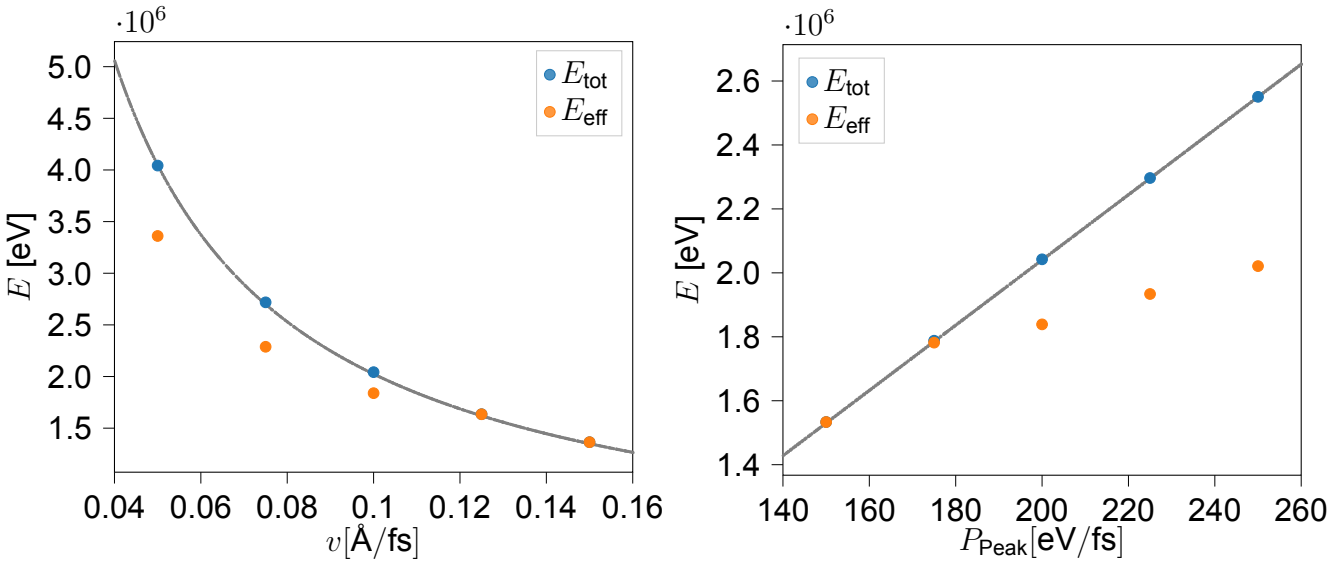

(a) $P = 200\,\text{eV/fs}$ (b) $v = 0.1\,\text{Å/fs}$

Figure 4.7: The total energy E_{tot} and the effective energy E_{eff} is plotted for different laser velocities (a) and different laser power (b). The gray lines show the theoretical total laser energy under the condition of complete absorption, arising from the laser parameter input. For differing speed and differing laser velocity, the absorbed energy behaves like $E_{\text{tot}} \propto P$ and $E_{\text{tot}} \propto 1/v$.

slope is different for the change in velocity and the change in laser power. The vaporized energy increases more rapidly as the laser power increases than as the laser velocity decreases.

Figure 4.8(b) shows the aluminum fraction ordered in FCC structure during laser penetration for selected laser parameters. The fraction of FCC structure decreases with the increase of temperature in the sample, see fig. 4.6, caused by the laser penetration. The decrease of the FCC structure for different laser parameters differs only in the total decrease, while the course relative to the laser position is the same for all laser parameters. This shows that the evolution of the FCC structure in the sample depends only on the applied energy and not on the specific power or velocity parameter. After the laser leaves the sample, the fraction of FCC structure does not change significantly.

These two deductions from the fraction of FCC structure remain in contrast to the melting dynamics described in section 4.1. It has been shown that at higher laser velocities the melting dynamics starts after the laser has left the sample. The FCC structure, on the other hand, breaks during laser penetration and remains constant after the laser has left the sample. The reason for this is that the breaking of the FCC structure starts directly with the energy rescaling of the atoms caused by the laser penetration. The observed deformation of the sample, on the other hand, takes place on the time scale of phonon relaxation. This also explains the constant FCC fraction after laser penetration. As large parts of the sample melt, the FCC structure on the atoms involved is already broken during the laser interaction. In addition, the breaking and formation of FCC due to head transfer within the sample tent is

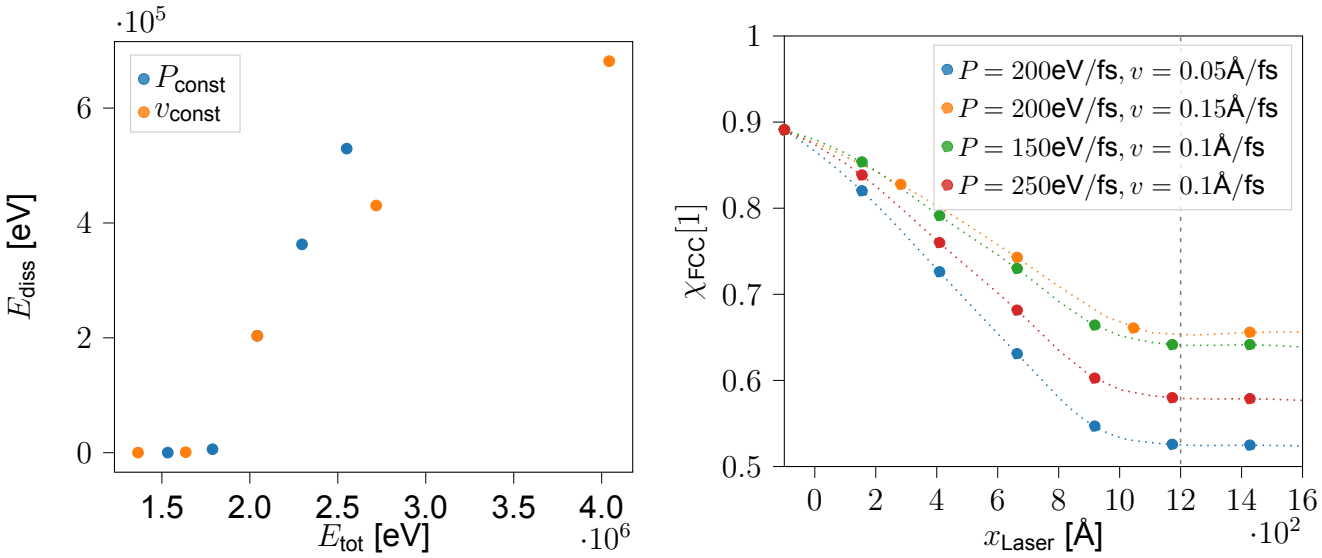

(a) $P = 200\,\text{eV/fs}$ (b) $v = 0.1\,\text{Å/fs}$

Figure 4.8: The disappeared energy E_{diss} id plotted for different applied laser energies, for changing laser speed and laser velocity in Figure(a). Figure (b) shows the breaking of the FCC structure, while laser penetration for different laser parameters. The friction χ_{FCC} is plotted over the laser position.

largely balanced, as shown in fig. 4.8(b).

4.1.2 Parameter Comparison to Experiments

Before performing the simulation of the PBF process, it is necessary to have a look at the setup of the sample as well as the way to a reasonable parameter set. For this purpose, two experimental parameter sets are scaled down to simulation size.

In the experiments on Olakanmi [21], layers with a thickness of $d = 0.25$ mm were scanned at a speed of $v =$ 50-150mm/s, a power of P= 100-240W and a scan spacing of $s = 0.1$ mm. Pure aluminum and various aluminum alloys were used in this experiment. PBF experiments with a layer thickness of $d = 10\,\mu m$ were done by An [22] on stainless steel. The laser parameters in these experiments are velocity v =100 mm/s, power P= 50 W and scan spacing $s = 40\,\mu m$.

In the units of our simulation, P in [eV/10.18fs] an v [Å/fs] we get the conversion rates of

$$1\text{W} = 1\frac{\text{J}}{\text{s}} = 1 \cdot \frac{6.242 \cdot 10^{18}\text{eV}}{\frac{10^{15}}{10.18} \cdot 10.18\text{fs}} = 6.354 \cdot 10^4 \frac{\text{eV}}{10.18\text{fs}}$$

$$1\frac{\text{mm}}{\text{s}} = 1 \cdot \frac{10^7\text{Å}}{\frac{10^{15}}{10.18} \cdot 10.18\text{fs}} = 1.018 \cdot 10^{-7} \frac{\text{Å}}{10.18\text{fs}}.$$

In the simulation, the scan distance of $s = 400\,\text{Å}$ is modeled by the y-dimension of the simulation box. The layer thickness is composed of the molten powder as well as the molten part of the soil, with a target size of $d = 200 - 300$Å. The parameters used in fig. 4.1 are not directly from the experiment, but from previous smaller simulations to reproduce the

	laser speed P	laser power v
Olakanmi [21]	$6.354 - 15.2496 \cdot 10^6 \frac{\text{eV}}{10.18\text{fs}}$	$5.09 - 15.27 \cdot 10^{-6} \frac{\text{Å}}{10.18\text{fs}}$
An [22]	$3.177 \cdot 10^6 \frac{\text{eV}}{10.18\text{fs}}$	$10.18 \cdot 10^{-6} \frac{\text{Å}}{10.18\text{fs}}$
Simulation	$1500 - 2500 \frac{\text{eV}}{10.18\text{fs}}$	$0.5 - 1.5 \frac{\text{Å}}{10.18\text{fs}}$

	energy density $P/(v \cdot s)$	layer thickness d
Olakanmi [21]	$4.161 - 29.98 \cdot 10^5 \frac{\text{eV}}{\text{Å}^2}$	$2.5 \cdot 10^6$Å
An [22]	$7.802 \cdot 10^5 \frac{\text{eV}}{\text{Å}^2}$	$1 \cdot 10^5$Å
Simulation	$3.3 - 10 \frac{\text{eV}}{\text{Å}^2}$	$200 - 300$Å

Table 4.1: Experimental laser parameters compared to the simulation parameters form this work in the units of the simulation scale.

macroscopic dynamics of PBF.

Table 4.1 lists the laser values for experiment and simulation in the scale of the simulation. The higher laser power combined with the slower laser velocity results in a higher energy density transferred to the sample as well as a larger layer thickness compared to the simulation.

4.1.3 Powder Property Comparison

Besides the laser parameters, the powder configuration plays an essential role in the properties of the final sample, as explained in section 2.1.3. To analyze the influence of different powder properties, a melting and recrystallization process of three samples with different distributions of coarse and fine particles is simulated. The laser parameters for all three samples are given by laser power $P_{\text{Laser}} = 2500\,\text{eV}/10\,18\text{fs}$ and velocity $v_{\text{Laser}} = 1.0\,\text{Å}/10\,18\text{fs}$. At $200\,\text{ps}$ after laser penetration, the sample cooled to $k_\text{b}T = 0.0235\,\text{eV}$ with the cooling rate of $\text{d}(k_\text{b}T)/\text{d}t = 1.21 \cdot 10^{-3}\,\text{eV/ps}$.

The structure of each sample after laser penetration or recrystallization is shown in fig. 4.9. The melted samples differ between the powder sample *coarse00* and the powder samples *coarse015* and *coarse025*. The molten structure of samples *coarse015* and *coarse025* consists of a continuous layer of molten aluminum causing gas inclusion. Several solid grains remain below the liquid layer. The *coarse00* sample, on the other hand, melts into a fountain that does not fill the entire xy-plane of the simulation box. There are no closed gas pockets. All grains in this sample are molten, as recrystallization on the bottom can be observed even before the sample cools.

The different melting forms are due to the sample properties. While sample *coarse00* contains grains with only Gaussian distribution, the other samples contain both fine and coarse particles. This leads to a more uniform melting behavior in sample *coarse00*, which results in a large fountain. The different grain sizes in samples *coarse015* and *coarse025* lead to a uniform melting behavior only on the surface of the sample, which causes the molten layer.

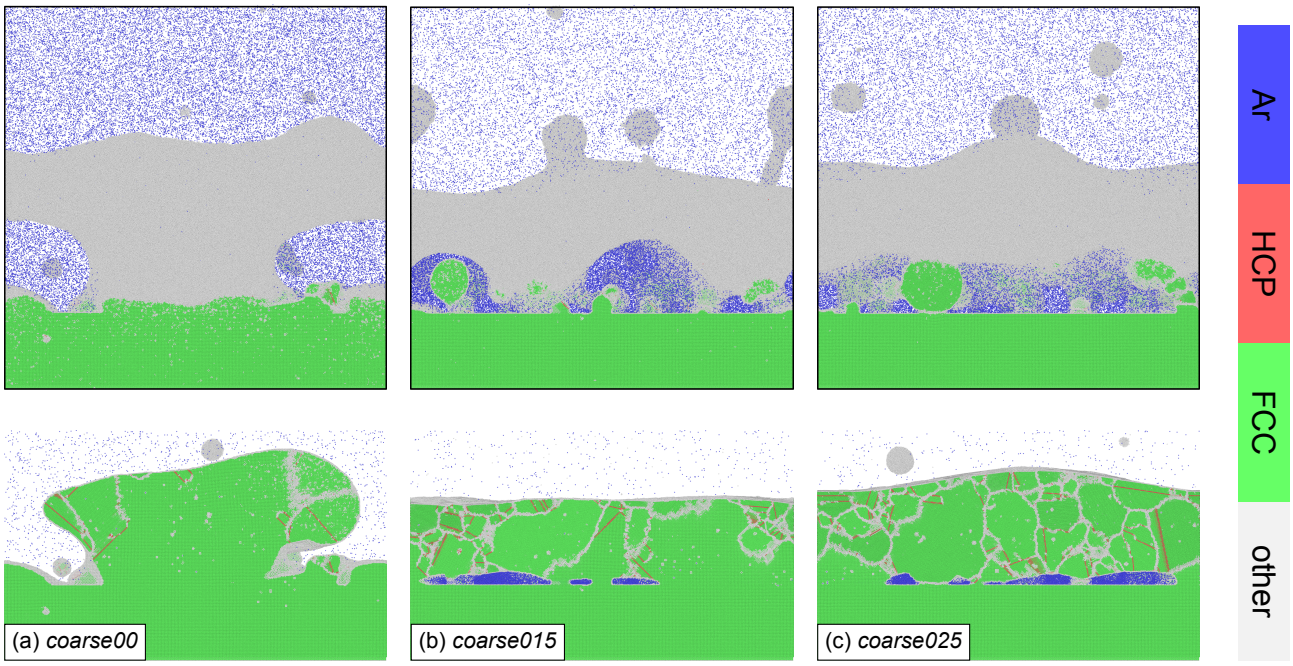

Figure 4.9: The structure of the three powder samples *coarse00*, *coarse015* and *coarse025* according to table 3.1 after the laser penetration (top) and after complete recrystallization is shown.

Table 4.2: The fraction of FCC structure within each sample after the laser penetration as well as after the recrystallization is listed.

cooling rate $\mathrm{d}(k_\mathrm{b}T)/\mathrm{d}t$ [eV/ps]	χ_{FCC}, molten	χ_{FCC}, solid
coarse00	0.537	0.922
coarse015	0.528	0.897
coarse025	0.512	0.893

The small differences in the FCC structure after laser penetration, listed in table 4.2, can be explained by the visually different number of atoms for the three samples, see table 3.1.

The liquid fountain shape of *coarse00* leads to an uneven solid sample after cooling as shown in fig. 4.9(a). The finite cooling time prevents the liquid aluminum from solidifying, resulting in a droplet above the bottom. The *coarse015* and *coarse025* samples compress the trapped gas and form a more uniform surface. The large curvature of the surface of *coarse025* compared to *coarse015* is due to the higher amount of coarse particles in the sample, which leads to less uniform melting. The structure for *coarse00* is less fractured, resulting in the highest proportion of FCC structure. The other samples show a more fractured structure, as one can get interruptions of the FCC structure due to the gas pockets. Especially for the *coarse025* sample, the fractured structure is caused by the small contact area between the liquid aluminum and the solid ground.

4.2 Recrystallization Behavior

In order to analyze the sample properties as a function of the selected parameter set, the sample must first recrystallize. The first part of this section discusses the recrystallization process of a uniformly molten sample and an incompletely molten sample. In the second part of this section, the influence of the cooling rate on the resulting sample is analyzed.

4.2.1 Sample Crystallizing Comparison

The initial configuration after the PBF process for the completely molten sample without any surrounding gas is shown in fig. 4.10(a). A molten sample with gas pockets in the melt is shown in fig. 4.11(a) as well as a barely molten sample in fig. 4.12(a). The sample temperature is then controlled using an NH thermostat with a cooling rate of $\mathrm{d}(k_\mathrm{b}T)/\mathrm{d}t = 0.0002\,\mathrm{eV/fs}$. The images fig. 4.10 (b) - (d),fig. 4.11 (b) - (d) and fig. 4.12 (b) - (d) show the process after reaching the constant target temperature of $k_\mathrm{b}T = 0.023\,\mathrm{eV}$.
The atomistic structure of the fully molten sample without surrounding gas after the sample has reached the target temperature is shown in fig. 4.10(b). The melt on the top of the sample crystallizes onto the lattice structure of the unmelted sample. Small defects within the FCC structure result from the finite cooling rate.

A new crystallization behavior can be observed in fig. 4.10(c), after 100 ps. In the upper part of the sample, the nucleation of FCC structures from the unstructured liquid is shown. This structure formation leads to multiple separate FCC clusters with random orientation, resulting in a large fraction of non-regularly structured edge regions. Furthermore, the formation of HCP planes within the FCC grains is shown in fig. 4.10(c). The formation of defect planes in aluminum for rapid cooling is in good agreement with previous work [55].

For a longer time at the target temperature, the sample crystallization from the bottom and the previously formed grains continues until the grains contact each other as well as the bottom, see fig. 4.10(c). The large amount of unstructured material in this figure results from fine nucleation with different orientations combined with the operation of the CNA. The developed rough boundaries between the grains avoid the definition of a regular structure from the common neighbors. For a longer time scale of the simulation, as well as for an annealing at a temperature close to the melting temperature, the formation of larger grains is expected [56]. For annealing on the timescale of hours, grain sizes up to several micrometers, corresponding to the size of the simulation cell, are measured in the experiment [56].

The structure of the completely molten sample including the surrounding gas when reaching the target temperature is shown in fig. 4.11(b). The enclosed gas is spread out in the xy-plane and compressed by the influence of gravity section 3.4. Crystallization also occurs on existing FCC structures, but the direction of crystallization is strongly influenced by the location of the gas pockets. The decrease of the gas density above the sample is caused by the reflection at the top of the simulation box section 3.3 and has only a small influence on

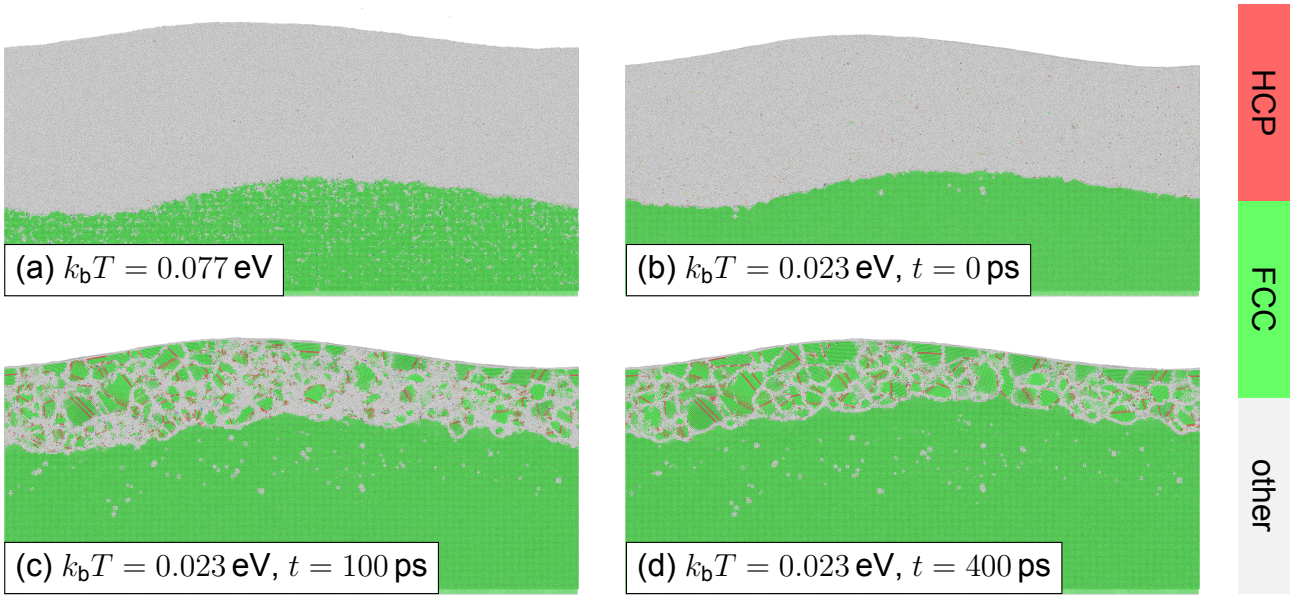

Figure 4.10: The crystallization process for a completely molten sample for a simulation without surrounding gas after induced by external cooling. While T describes the current temperature of the sample and t shows the time from reaching the target temperature of $k_bT = 0.023$ eV. The color of the atoms describes their lattice structure.

the dynamics.

After a time of $t = 100$ ps at the target temperature, the growth of grains around the gas pockets begins. As seen in fig. 4.11(c), the presence and shape of gas pockets can be a source of HCP defect structures within the crystallized sample. Further away from the bottom, nucleation from molten material takes place as shown in fig. 4.10(c).

The fully crystallized sample is shown in fig. 4.11(d). While the fraction of very small grains is relatively small compared to fig. 4.10(c), the crystalline structure resulting from the ground sample shows multiple cracks caused by gas pockets. Compared to the simulation without gas, the deformation of the gas pockets within the sample results in a more uniform surface.

The lattice structure of the not fully molten sample after external temperature reduction is shown in fig. 4.12(b). While the sample has several nuclei of not-molten powder, the crystallization occurs primarily from these existing structures. The overall shape of the sample does not change significantly in this case due to the high fraction of unmelted powder as well as the lower temperature of the melted part of the sample compared to the previous simulations, which leads to a lower mobility.

After $t = 100$ ps, the epitaxial growth of the grains becomes visible, see fig. 4.12(c). It can be seen that spontaneous nucleation from melting takes place, while smaller grains limit the expansion of growth from larger grains. It is also clear that HCP defect planes are more likely to occur in new nuclei than in structures caused by unmelted grains. The formation of the HCP structure comes from an energy that is close to the energy of the preferred FCC structure [36].

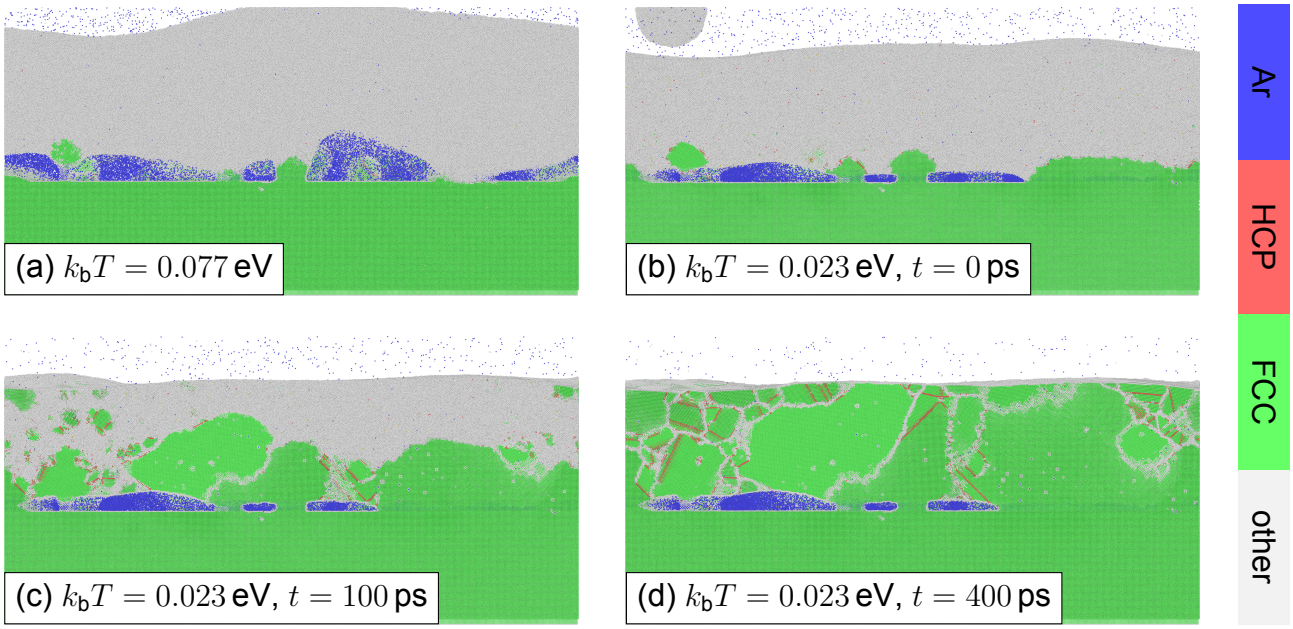

Figure 4.11: The crystallization process for a not complete molten sample after induced by external cooling. While T describes the current temperature of the sample and t shows the time from reaching the target temperature of $k_bT = 0.023$ eV.

The fully crystallized sample is shown in fig. 4.12(d). The process of grain growth in this sample, even for new nuclei, is in a much more advanced state compared to fig. 4.11(d) and fig. 4.10(d). Despite observing the same simulation time and cooling rate for all samples, the starting temperature of each sample plays a crucial role in the time scale to the dynamics in melting, leading to further crystallization and grain growth for samples with colder starting temperature.

The crystallization for the three samples is dominated by spontaneous crystallization and epitaxial growth from existing FCC structures. The time scale of spontaneous nucleation at less than $t = 50$ ps after reaching the target temperature agrees with results from quasi-2D simulations on the same topic [57]. Furthermore, the formation of HCP defect planes agrees well with previous MD work [55].

Crystallization for a not completely molten sample leads to the formation of a large drop over the sample instead of a uniform surface. In addition to a potentially rough surface, melting more layers onto such a sample can lead to huge porosity, while the powder may not be able to reach all the voids around the sphere.

The two fully melted samples show quite similar results in terms of melting dynamics, with two main differences. First, the layer of small lattice grains on top of the sample is much larger for the sample without surrounding gas. Secondly, the structure grown from the bottom is interrupted by the gas pockets for the sample with surrounding gas, while the sample without surrounding gas forms a uniform lattice in this region. The influence on the stress resistance is discussed in section 4.3.

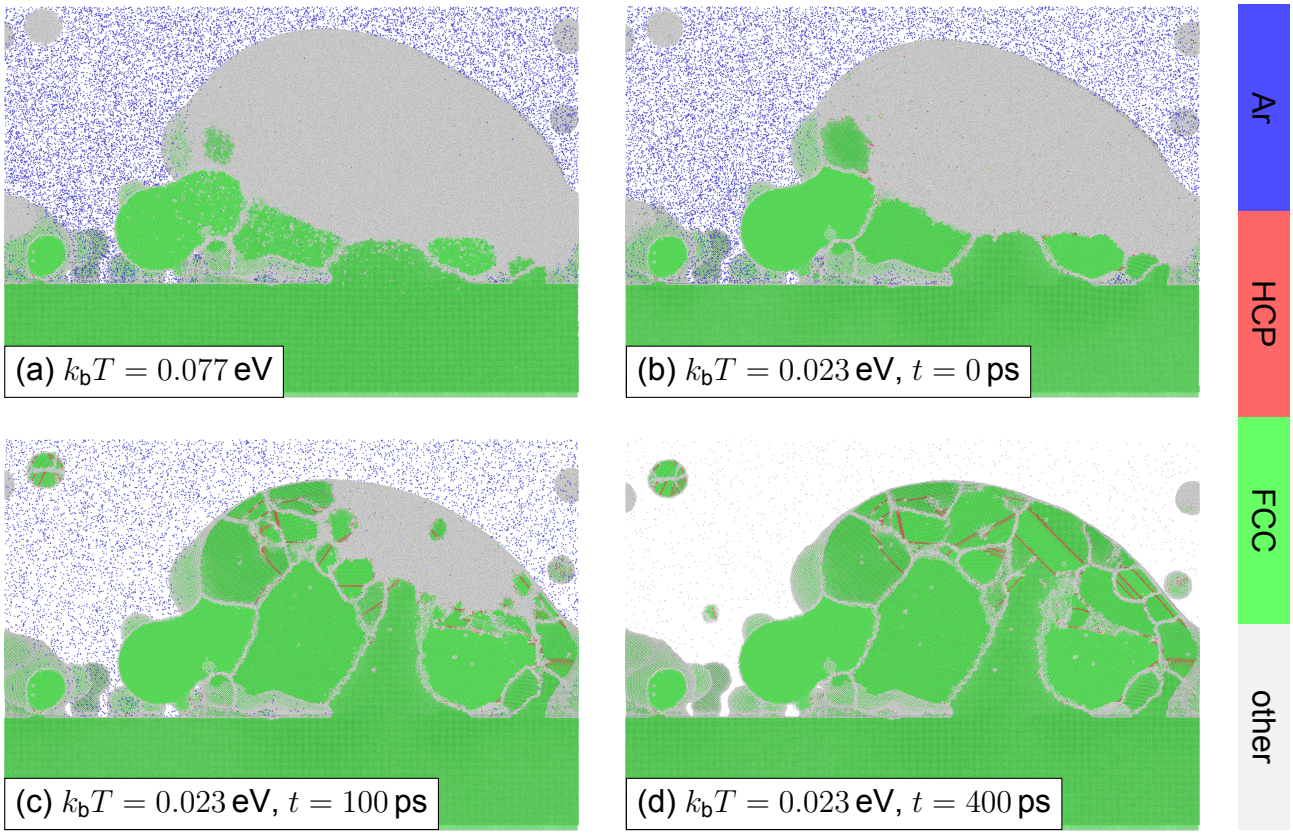

Figure 4.12: The crystallization process for a not complete molten sample after induced by external cooling. While T describes the current temperature of the sample and t shows the time from reaching the target temperature of $k_bT = 0.023$ eV.

4.2.2 Cooling Rate Comparison

After understanding the basic mechanisms in the crystallization process, the influence of the cooling rate on the sample is discussed in this section using the sample fig. 4.11(b). The cooling rates in the table 4.3 are derived from previous MD work in the field of PBF [57] as well as general work on aluminum crystallization [55]. Experimentally realizable cooling rates are in the range of $1 \cdot 10^{-16}$ [eV/ps] to $1 \cdot 10^{-12}$ [eV/ps] [58]. Although the macroscopic cooling is several orders of magnitude larger than in the MD simulation, a general understanding of the influence of the cooling rate on the crystallization behavior is approached. Even at a much slower macroscopic cooling rate, local cooling rates in a process far from thermal equilibrium can differ greatly from the macroscopic cooling rate, e.g. by contact with colder material from a previous layer due to strong convection.

Figure 4.13 shows the lattice structure of for different cooling rates at time $t = 205$ ps. Faster cooling rates lead to the formation of smaller grains of the FCC structure. As shown in fig. 4.13(a), especially above the gas inclusions, very small powder grains have formed, for a slower cooling rate, the grain size increases due to the reduction of spontaneous nucleation within the melt. In addition, at slower cooling rates, the gas is further compressed and can partially escape. For the slowest cooling rate, shown in fig. 4.13 (d), the least number of HCP defect planes have formed.

Table 4.3: The cooling rate $\mathrm{d}(k_\mathrm{b}T)/\mathrm{d}t$ of the sample and the resulting fraction of FCC structure $610\,\mathrm{ps}$ after the start of the cooling process.

$\mathrm{d}(k_\mathrm{b}T)/\mathrm{d}t$ [eV/ps]	χ_{FCC}
$6.09 \cdot 10^{-4}$	0.936
$1.21 \cdot 10^{-3}$	0.897
$2.42 \cdot 10^{-3}$	0.890
$1.21 \cdot 10^{-2}$	0.874

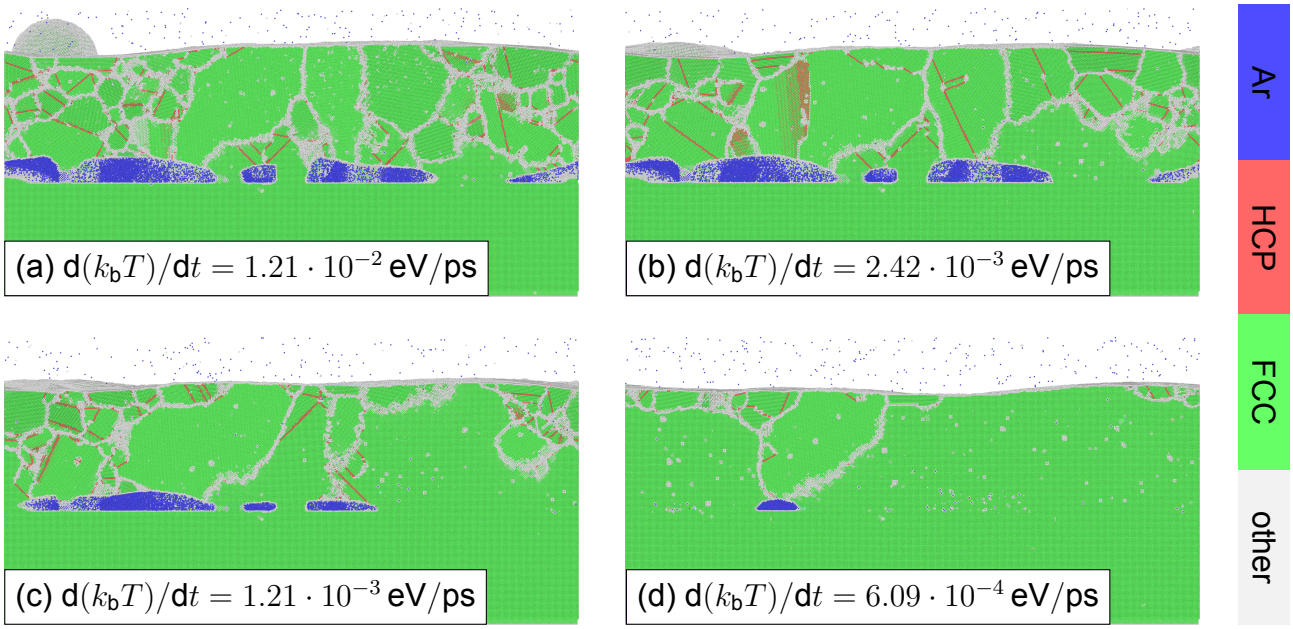

Figure 4.13: Recrystallization of sample fig. 4.11 for different cooling rates to a target temperature of T = 0.023 eV after a time of t = 305 ps for the beginning of the cooling process.

The crystallization process can also be followed by analyzing the fracture of the FCC structure in the sample, shown in table 4.3. There is a direct correlation between the cooling rate and the fracture of the FCC structure within the sample. For slower cooling, the fracture of the FCC structure increases. For faster cooling, the HCP structure within the defect planes and the amorphous structure between the different FCC grains have a higher fraction within the sample.

These results on the dependence of the cooling rate on the sample structure are in agreement with previous work [50]. For a further increase of the cooling rate, the fraction of amorphous structure is expected to increase, since faster cooling rates deviate even more from the experimental values.

4.3 Stress Application

To quantify the mechanical properties of the resulting specimen, a deformation stress can be applied to the specimen. The deformation is performed as described in section 3.7. The upper part of the sample is moved with the deformation rate $v_{\text{def}} = 1 \cdot 10^{-2}\,\text{Å}/10.18\text{fs}$ for all following tension, compression and shear simulations. The deformation simulations will focus on the influence of gas inclusions on the mechanical properties. The sample without gas inclusion is discussed in fig. 4.10 and the sample with gas inclusion is discussed in fig. 4.11.

The atomic structure of the sample with gas inclusion under tension is shown in fig. 4.14. Pulling on the upper part of the sample leads to a fracture of the sample in the plane between ground and printed powder, in which gas pockets appear. For smaller strain (fig. 4.14(a)), bending of the FCC lattice can be observed. As the strain applied to the sample increases, the FCC structure begins to fracture (fig. 4.14(b)). After the two parts are completely pulled apart, the FCC structure on each side reforms as the stress on the lattice disappears (fig. 4.14(b)).

The atomic structure of the sample including the gas during compression is shown in fig. 4.14. During compression of the sample, the gas within the sample is completely compressed before the aluminum structure is deformed. As one can see the difference in the deformation of the bottom structure below a gas pocket compared to parts where no gas is compressed, see fig. 4.14 (a) and (b). Further compression results in the formation of planes of HCP structure within the sample. The FCC-HCP transition in aluminum under pressure in the order of GPa is mountainous in the reduction of volume per atom in the HCP structure compared to the FCC structure.

The shear deformation in x-direction is shown in fig. 4.16. For the sample with gas, the shear deformation results in a fracture for the structure between ground and printed powder, as seen for the tensile simulation. The stress on the sample causes the formation of HCP structures in the sample, as shown in fig. 4.16 (a) and (b). In comparison, the shear deformation of the sample without gas is mainly due to deformation in the upper part, including small aluminum grains. In this case, no fracture of the structure can be observed, while the bending of the FCC structure is visible, see fig. 4.16 (c) and (d).

The stress-strain relationship for the sample with gas as well as the sample without gas for tensile, compression and shear stress is shown in fig. 4.17. The amount of stress, calculated as the normal force on the moving part of the sample, is shown in units of GPa to compare the results with previous work on the stress resistance of PBF samples.

Figure 4.17(a) shows the stress-strain curve for the tensile simulation. For the sample without gas, stress values up to $2.4\,\text{GPa}$ are reached, while the sample with gas inclusion reaches the maximum stress of $0.6\,\text{GPa}$ before the stress is released by fracture. The characteristic of the stress-strain curve for the sample without gas is comparable to previous experimental work [53] on this topic as well as MD simulations in two dimensions [57] and three dimensions [59]. The stress grows with increasing strain until it reaches the ultimate tensile strength before the stress is released by fracture. The stress growth is interrupted

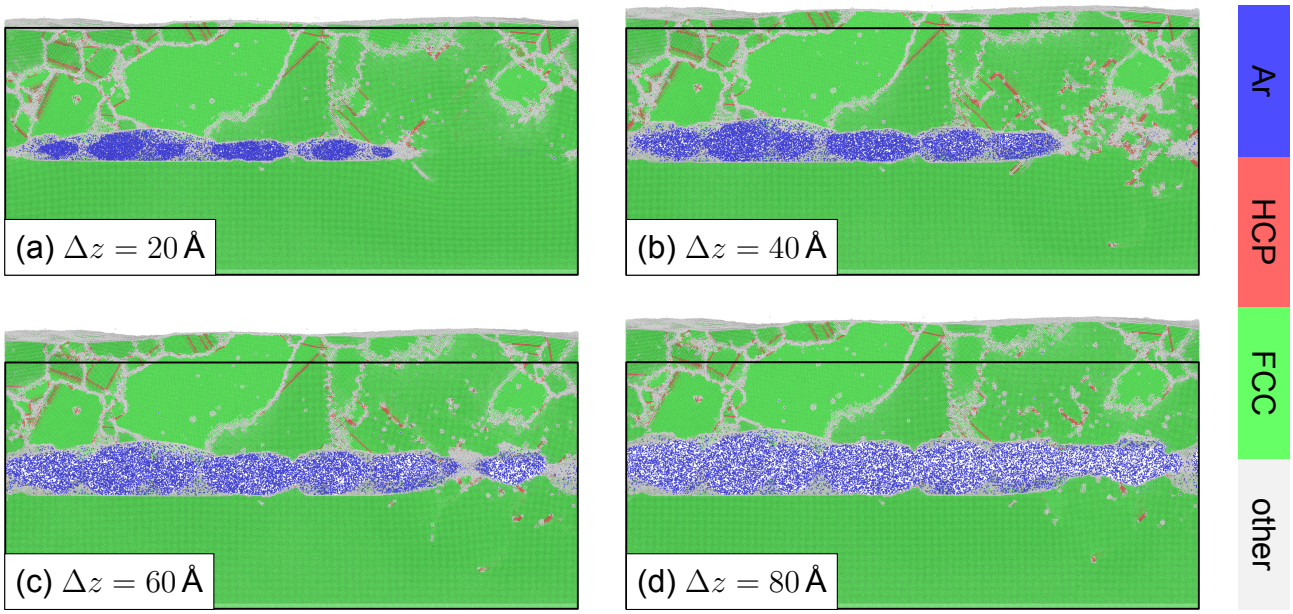

Figure 4.14: Lattice structure of a sample with gas pockets, while appending tension. The upper part of the sample is pulled constantly in positive z-direction by the margin Δz, while the ground is fixed.

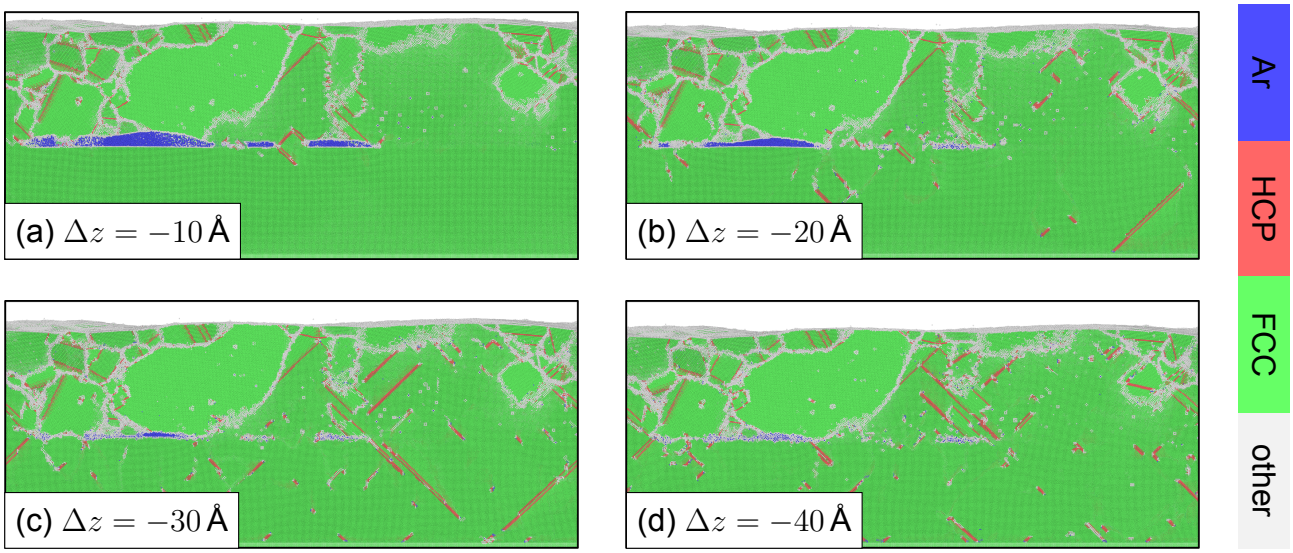

Figure 4.15: Lattice structure of a sample with gas pockets, while compressing. The upper part of the sample is compressed constantly in negative z-direction by the margin Δz, while the ground is fixed.

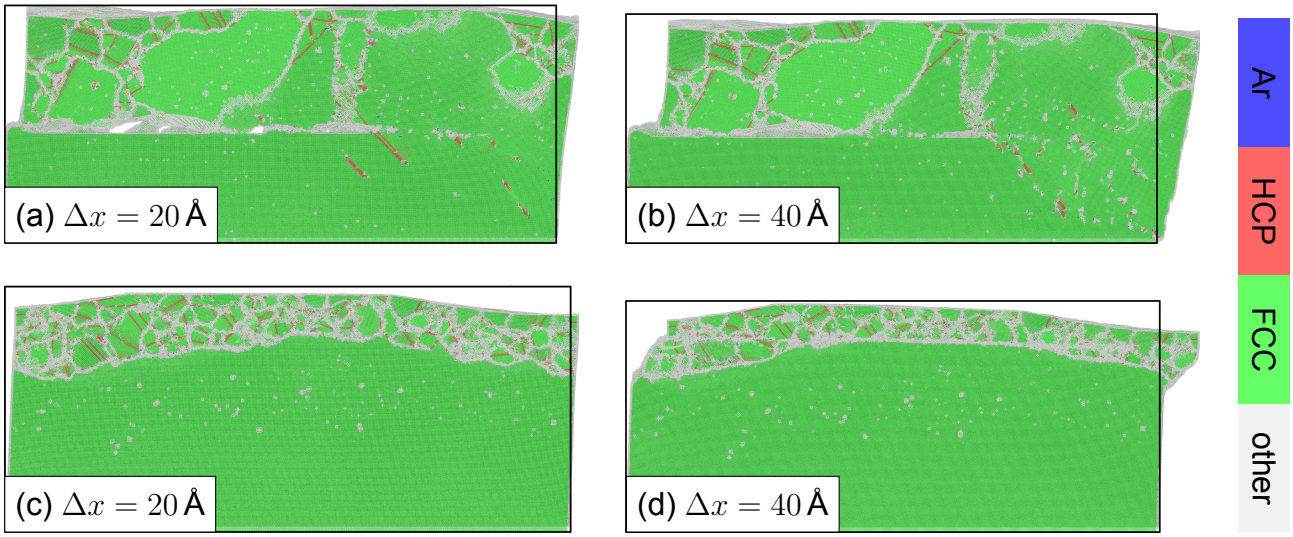

Figure 4.16: Lattice structure of a sample with gas pockets, while appending shear stress. The upper part of the sample is pulled constantly in positive x-direction by the margin Δz, while the ground is fixed. The sub-figures (a) and (b) refer to sample with gas inclusion, while the figures (c) and (d) refer to a sample without gas inclusion.

by two partial relaxations, which cause the stress to collapse for a short time. These irregularities are also seen in the experiment, although the relative magnitude in the experiment is much smaller [53]. The collapse of the stress within the simulation is due to the stress being out of equilibrium. This results in even negative stress values. The yield strength, which describes the threshold for elastic deformation, is not observed in this simulation or experiment at 273 K due to the low elasticity of aluminum at room temperature. The ultimate tensile strength of 2.4 GPa and the associated stress are in agreement with previous MD simulations on equiaxed grain aluminum [59]. The experimental results show a lower ultimate tensile strength and a higher associated strain, corresponding to the slower deformation and a sample size in the order of millimeters. The gas-filled specimen does not show comparable characteristics. The stress-strain curve shows several partial fractures, with the stress decreasing with each fracture.

Figure 4.17(b) shows the stress-strain curve for the compression of the sample. For both specimens, the stress magnitude increases with increasing strain due to the continuous compression of the specimen. The stress increases stepwise with strain. This behavior is also observed for the simulation of the compression of aluminum nanowires in a less distinct shape [60]. The extreme step shape in this case is due to simulation out of equilibrium. The curves for the sample with and without gas tend to be shifted along the strain axis. This is due to the compression of the trapped gas inside the sample, whereas once the gas is fully compressed, the stress-strain behavior for both samples is the same.

The stress-strain curve for shear stress is shown in fig. 4.17(c). The applied stress in this simulation is an order of magnitude smaller than in the tensile simulation. The rapid decrease in stress at a deformation of 15 Å for the sample with gas indicates fracture in the structure, while the stress for the sample without gas does not indicate fracture formation.

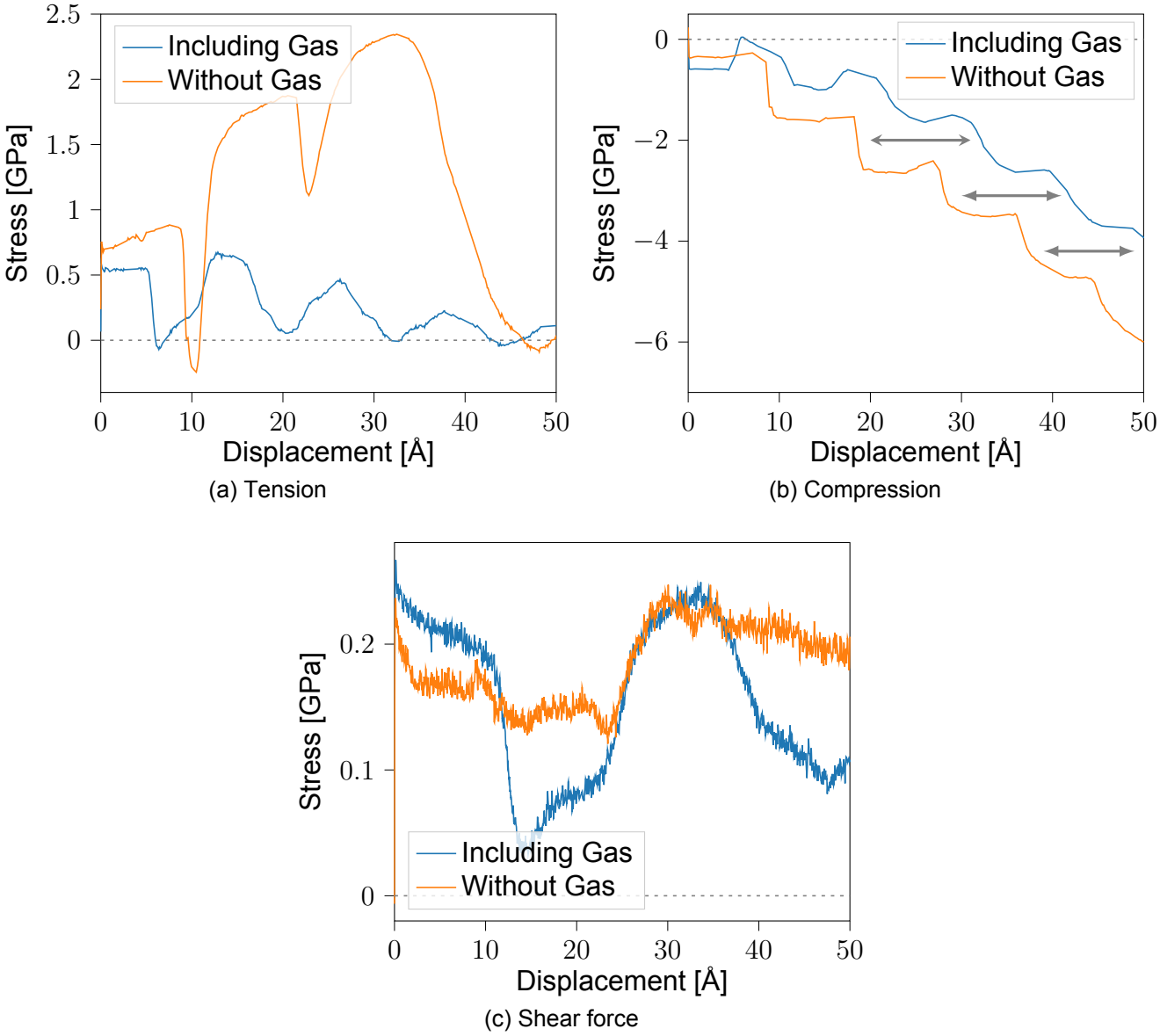

Figure 4.17: The pressure from normal force of the stress test is illustrated. The subplots refer to the simulations: (a) to fig. 4.14, (b) to fig. 4.15 and (c) to 4.16.

Chapter 5

Summary and Outlook

5.1 Summary

Nanoscale PBF simulations using molecular dynamics provide an efficient way to analyze the malting and crystallization within the PBF process to gain knowledge of the microstructure and laser penetration on an atomistic basis. In this work, the PDF process of pure aluminum is investigated. Since there are several alloys that are more relevant for manufacturing, this thesis aims to build a framework that allows the analysis of the PBF process of various samples containing alloys and elementary metals.

The simulation framework includes every step from the creation of a powder sample to the quantification of the stress properties of the resulting sample. The creation of the samples is based on the experimental sample using a distribution of particle sizes. This allows a comparison between different properties for the powder by changing the particle size distribution. The laser penetration of the sample is modeled on an atomistic basis, where the kinetic energy is recovered. The laser absorption depends on the particle density and even allows the calculation of a mixed absorption coefficient for further studies on alloys. During the laser penetration, the MD simulation provides atomistic energy properties not accessible by FEM simulations. Surrounding gas leading to gas pockets in the sample is modeled in order to transfer the macroscopic properties of the atomistic simulation. The NH thermostat is used to force crystallization of the molten sample after laser penetration. The change of cooling rates as well as the visualization of the lattice structure within the sample during the crystallization process allows a closer insight into the different mechanisms of lattice structure formation. By deforming the sample, the influence of gas pockets on the mechanical properties and the evolution of the lattice structure within the sample can be shown.

The melting behavior is compared for different laser properties and powder compositions. For the laser penetration, an ablation threshold of the locally averaged intensity $I_{\text{th}} = 5\text{eV}/\text{Å}^2$ can be defined for the total laser penetration. Below this threshold, the powder particles melt onto each other. Higher laser intensities cause the injection of fountains and droplets, leading to energy and material losses. A laser intensity above this threshold results from an increase in laser power caused by a decrease in laser velocity. The vaporized energy, which

causes a reduction in the effective energy responsible for melting within the sample, shows a higher increment when the total energy is increased due to a higher laser power compared to the reduction in laser velocity. Furthermore, the heat distribution during the laser penetration shows a high fraction of heat convection for a slower laser velocity, which is related to the phonon relaxation time of aluminum. The comparison of powder samples shows a more uniform melting for powder particles of the same size compared to powder samples with highly different particle sizes. The lower powder density for the same size particles results in a single fountain melt shape, while samples with different powder particle sizes result in a mostly flat melt surface with gas inclusions.

The crystallization of the sample shows two different mechanisms of lattice formation. The growth of non-molten structures results from the soil layer and powder particles with residual FCC structure. As existing structures grow with their original orientation, different orientations lead to amorphous boundaries. Spontaneous nucleation from the melt occurs in areas not close to existing FCC structures. This results in the formation of randomly oriented grains. The size of the grains formed increases with slower cooling as the proportion of spontaneous nucleation decreases. This leads to a decrease in the FCC structure with faster cooling. Within the grain formation, HCP defect planes occur as this behavior also increases with faster cooling of the sample. Trapped gas is further compressed and is able to partially escape from a slower melting, leading to a more dense sample.

Mechanical properties are studied by deforming the sample and tracking the induced stress. Samples with gas pockets show significantly weaker mechanical properties compared to the same generated sample without surrounding gas within the simulation. Both additive fabricated specimens show partial fracture in tensile tests before complete fracture.

5.2 Outlook

This work opens up further investigations in the field of MD simulation as well as the transfer of knowledge for MD simulation to larger scaled FEM simulations.

The work on an atomistic basis becomes even more relevant for the study of alloys, as a greater variety of structures and their formation can be further investigated. A combination of this work on powder samples and the work of Vietz [38] on TiAl alloys and even extending the range of metals and alloys may provide useful results. Furthermore, the melting of an additional layer on top of the crystallized sample and the fusion of both layers may be of interest, as this has only been observed in two dimensions on an atomistic basis [57].

Besides the simulation of single atoms, the framework can be used for coarse-grained models. Pseudo-atoms, which are approximate groups of atoms, can be used to extend the size and time scale of the simulation. The challenge for this approach is to create a reasonable potential for the pseudo-atoms in order to correctly reproduce the physical properties of the metal or alloy.

Since FEM simulations rely on several assumptions, results from MD simulations can be

used to further improve the physical description in FEM simulations. The evaporated energy at the atomic level, the grain size and the resulting mechanical properties as a function of cooling rate are possible inputs for FEM simulations.

5.3 German Summary

Additive Fertigung (AM) ist auf dem Vormarsch, und das nicht nur wegen der kontinuierlichen Steigerung der Kosteneffizienz und der Verkürzung der Produktionszeit. Herkömmliche Fertigungsverfahren stoßen an ihre Grenzen, wenn es um komplexe Geometrien und komplizierte Strukturen innerhalb von Bauteilen geht [2].

Während AM bzw. 3D-Druck im Allgemeinen meist mit dem Druck von Polymeren in Verbindung gebracht wird, gewinnt das Drucken von Metallen und Legierungen aufgrund ähnlicher Vorteile zunehmend an Bedeutung für kommerzielle Anwendungen. In diesem Zusammenhang werden laserinduzierte AM-Verfahren wie Pulverbettschmelzen (PBF) und selektives Lasersintern (SLS) aufgrund der hohen Auswahl von Materialien, einschließlich Polymeren, Metalllegierungen und Keramiken, immer wichtiger. Insbesondere PBF kann sehr dichte Metallteile mit hervorragenden mechanischen Eigenschaften liefern. Darüber hinaus bietet PBF eine präzise Kontrolle über die Zusammensetzung der Bestandteile des hergestellten Bauteils [5]. Aufgrund des einstufigen Herstellungsverfahrens eignet sich PBF für Prototyping, da trotz Änderung des verarbeiteten Materials oder geringfügiger Größe des Größe des Bauteils in der Regel kein Werkzeug erforderlich ist [6].

Neben den Vorteilen gibt es jedoch auch einige Herausforderungen und Einschränkungen. Trotz der hohen Kosten für Ausrüstung und Infrastruktur im Zusammenhang mit PBF [7] besteht die größte Herausforderung in der Qualitätskontrolle und Reproduzierbarkeit [8].

Um den Ablauf des Prozesses zu optimieren und die resultirende Qualität des Bauteils zu verbessern, können Simulationen des Prozesses einen Einblick in bestimmte Versuchsparameter geben. Simulationen haben mehrere Vorteile gegenüber der experimentellen Analyse einer Reihe von Parametern. Einerseits werden durch das Testen von Parametern in einer Simulation die Materialkosten reduziert, andererseits ist der Iterationsschritt der Änderung von Parametern in einer Simulation kürzer und weniger arbeitsintensiv als die Änderung eines Versuchsaufbaus. Zusätzlich bieten Simulationes auch einige Vorteile für das Verständnis des Prozesses. Während Experimente nur das fertige Bauteil liefern, erlaubt eine Simulation einen genaueren Blick auf den Prozess selbst und liefert Informationen über den Ursprung der Eigenschaften des Bauteils. Auch strukturelle Eigenschaften einer Probe sind in einer Simulation besser zugänglich.

In dieser Arbeit wird der PDF-Prozess von reinem Aluminium untersucht. Zwar gibt es verschiedene Legierungen, die für die in der Anwendung relevanter sind. Diese Arbeit zielt darauf ab, einen Rahmen zu schaffen, der die Analyse des PBF-Prozesses verschiedener Proben ermöglicht, die Legierungen und elementare Metalle enthalten.

Die Simulation umfasst jeden Schritt von der Herstellung einer Pulverprobe bis zur Quantifizierung der mechaninschen Eigenschaften der resultierenden Probe. Die Erstellung der Proben basiert auf der experimentellen Proben unter Verwendung einer Verteilung der Partikelgrößen. Dies ermöglicht einen Vergleich zwischen Pulver Zusammensetzungen durch Änderung der Verteilung Partikelgrößen. Die interaktion zwischen Laser und Probe wird auf atomarer ebene modelliert, wobei die kinetische Energie skliert wird. Die Laserabsorption hängt von der Partikeldichte ab und ermöglicht zudem die Berechnung eines zusammendesetzen Absorptionskoeffizienten für weitere Untersuchungen an Legierungen. Das Schutzgas, welches zu Gaseinschlüssen inerhalb der Probe führt, wird so modelliert, dass die makroskopischen Eigenschaften des Gases reproduziert werden. Zur Kristallisation der geschmolzenen Probe nach der Laserpenetration wird die Probe mittels eines Nosé-Hoover Thermostats abgekühlt. Unterschiedliche Abkühlungsraten in Kombination mit der Visualisierung der Gitterstruktur innerhalb der Probe während des Kristallisationsprozesses ermöglichen einen näheren Einblick in die verschiedenen Mechanismen der Kistallisation. Durch die Verformung der Probe kann der Einfluss von Gaseinschlüssen auf die mechanischen Eigenschaften und die Entwicklung der Gitterstruktur innerhalb der Probe untersucht werden.

Das Schmelzverhalten wird für verschiedene Lasereigenschaften und Pulverzusammensetzungen verglichen. Für die Laserinteraktion kann eine Ablationsschwelle der örtlich gemittelten Intensität $I_{\text{th}} = 5\text{eV}/\text{Å}^2$ addiert über die gesamte Laserinteraktion definiert werden. Unterhalb dieses Schwellenwerts schmelzen die Pulverpartikel zusammen. Für Laserintensitäten oberhalb der Ablationsschwelle bilet das Aulminium Fontänen und Tröpfchen welche zu Energie- und Materialverlusten führt. Eine Erhöhung der Laserintensität wird durcheine Erhöhung der Laserleistung oder einer Reduktion der Lasergeschwindigkeit erreicht. Die verdampfte Energie, steigt bei der Erhöhung der Gesamtenergie durch eine höhere Laserleistung stärker, im Vergleich zur verdampfen Energie bei Verringerung der Lasergeschwindigkeit. Darüber hinaus zeigt die Wärmeverteilung während der Laserinteraktion einen hohen Anteil an Konvektion für eine geringere Lasergeschwindigkeit, was mit der Phononenrelaxationszeit von Aluminium zusammenhängt. Der Vergleich von Pulverproben zeigt ein gleichmäßigeres Aufschmelzen von Pulverpartikeln gleicher Größe im Vergleich zu Pulverproben mit sehr unterschiedlichen Partikelgrößen. Die geringere Pulverdichte bei gleich großen Partikeln führt zu einer Fontänenförmigen Schmelze, während Proben mit unterschiedlichen Pulverpartikelgrößen eine meist flache Schmelzoberfläche mit Gaseinschlüssen ergeben.

Die Kristallisation der Probe zeigt zwei unterschiedliche Mechanismen der Gitterbildung. Das Wachstum aus nicht geschmolzenen Strukturen. Da die vorhandenen Strukturen in ihrer ursprünglichen Ausrichtung wachsen, führen unterschiedliche Gitterausrichtungen zu amorphen Strukturen an den Grenzenflächen. Spontane Keimbildung aus der Schmelze findet in Bereichen statt, welche nicht in der Nähe der vorhandenen FCC-Strukturen liegen. Dies führt zur Bildung von zufällig ausgerichteten Gitterstrukturen. Die Größe der gebildeten Gitterstrukturen nimmt bei langsamerer Abkühlung zu, wobei auch der Anteil der spontanen

Keimbildung abnimmt. Dies führt zu einer Abnahme der FCC-Struktur bei schnellerer Abkühlung. Innerhalb der bebildeten FCC Strukturen treten HCP-Defektebenen auf, auch dieses Verhalten nimmt mit schnellerer Abkühlung der Probe zu. Bei langsameren Schmelzen wird eingeschlossenes Gas weiter komprimiert und kann teilweise entweichen, was zu einer dichteren Probe führt.

Die mechanischen Eigenschaften werden durch Verformung der Probe und dafür nötigen Karft charakteisiert. Proben mit Gaseinschlüssen zeigen deutlich schlechtere mechanische Eigenschaften als die Probe ohne Gaseinschlüsse. Beide additiv hergestellten Proben brechen in Zugversuchen schrittweise bevor sie vollständig brechen.

Diese Arbeit eröffnet weitere Untersuchungen auf dem Gebiet der MD-Simulation sowie die Übertragung der Kentnnisse aus MD Simulationen auf Finite Elemente (FEM) Simulationen in größerem Maßstab.

Die Arbeit auf atomistischer Basis ist speziell für die Untersuchung von Legierungen relevant, da eine größere Vielfalt von Strukturen und deren Bildung weiter untersucht werden kann. Eine Kombination aus dieser Arbeit an Pulverproben und der Arbeit von Vietz [38] an TiAl-Legierungen, sowie eine Ausweitung des Spektrums an Metallen und Legierungen könnte nützliche Ergebnisse liefern. Darüber hinaus könnte das Aufschmelzen einer zusätzlichen Schicht auf der kristallisierten Probe und das Verschmelzen beider Schichten von Interesse sein, da dies bisher nur in zwei Dimensionen auf atomistischer Basis beobachtet wurde [57].

Neben der Simulation von einzelnen Atomen kann das Framework auch für coarse-grain Modelle verwendet werden. Pseudo-Atome, d.h. Gruppen von Atomen, können verwendet werden, um die Größe und die Zeitskala der Simulation zu erweitern. Die Herausforderung bei diesem Ansatz besteht darin, ein angemessenes Potenzial für die Pseudo-Atome zu schaffen, um die physikalischen Eigenschaften des Metalls oder der Legierung korrekt wiederzugeben.

Da FEM-Simulationen auf diversen Annahmen beruhen, können Ergebnisse aus MD-Simulationen zur weiteren Verbesserung der physikalischen Beschreibung in FEM-Simulationen verwendet werden. Die verdampfte Energie auf atomarer Ebene, die Korngröße und die sich daraus ergebenden mechanischen Eigenschaften als Funktion der Abkühlungsrate sind mögliche Annahmen für FEM-Simulationen.

Appendix A: Sample Equilibrartion Example

For the sample equilibaration, the simulation time directly correlates with the state of the sample. As the goal is to reach long simulation times as efficient as possible, the timestep for the simulation is increased multiple times. The reason for the extremely short timestep at the beginning is the weak gas interaction, which can lead to locally high temperatures for larger timestaps in the beginning.

```
ntypes 2

total_types 3

restrictionvector  2  0 0 0

core_potential_file  ../potentials/ALAR_M_phi-0.01.pt
embedding_energy_file  ../potentials/ALAR_M_F.imd.pt
atomic_e-density_file  ../potentials/ALAR_M_rho.imd.pt

coordname          ../configs/coarse_025_g1e5.imd

cpu_dim            32 8 16

box_from_header 1

pbc_dirs           1 1 1

outfiles           equi_025/nvt_0.02

inv_tau_eta        1

simulation         1
ensemble           nvt
maxsteps           1000
```

```
timestep        0.001
starttemp       0.02    # starting temperature
endtemp         0.02    # ending temperature
checkpt_int     1000
eng_int         10


simulation      2
ensemble        nvt
maxsteps        5000
starttemp       0.02    # starting temperature
endtemp         0.02    # ending temperature
timestep        0.01
checkpt_int     1000
eng_int         10

simulation      3
ensemble        nvt
maxsteps        10000
timestep        0.02
starttemp       0.02    # starting temperature
endtemp         0.02    # ending temperature
checkpt_int     1000
eng_int         10

simulation      4
ensemble        nvt
maxsteps        50000
timestep        0.05
starttemp       0.02    # starting temperature
endtemp         0.02    # ending temperature
checkpt_int     10000
eng_int         10


simulation      5
ensemble        nvt
maxsteps        70000
timestep        0.1
starttemp       0.02    # starting temperature
```

```
endtemp         0.02    # ending temperature
checkpt_int     10000
eng_int         100


simulation      6
ensemble        nve
maxsteps        100000
timestep        0.1
starttemp       0.02    # starting temperature
endtemp         0.02    # ending temperature
checkpt_int     10000
eng_int         100


simulation      7
ensemble        nve
maxsteps        120000
timestep        0.2
starttemp       0.02    # starting temperature
endtemp         0.02    # ending temperature
checkpt_int     10000
eng_int         100


simulation      8
ensemble        nve
maxsteps        200000
timestep        0.5
starttemp       0.02    # starting temperature
endtemp         0.02    # ending temperature
checkpt_int     10000
eng_int         100


simulation      9
ensemble        nve
maxsteps        500000
timestep        1
starttemp       0.02    # starting temperature
```

```
endtemp          0.02    # ending temperature
checkpt_int      10000
eng_int          100
```

Appendix B: Two Pulse PBF

In experiment, pulsed laser are very common for PBF are very common. Despite the small size scale such a simulation seems to of interest. The results in fig. 5.1 shot, that in the case of a completely melting of the powder, the dynamics does not differ much from the simulations with a moving laser spot, as convective heat distribution becomes relevent, as one would expect.

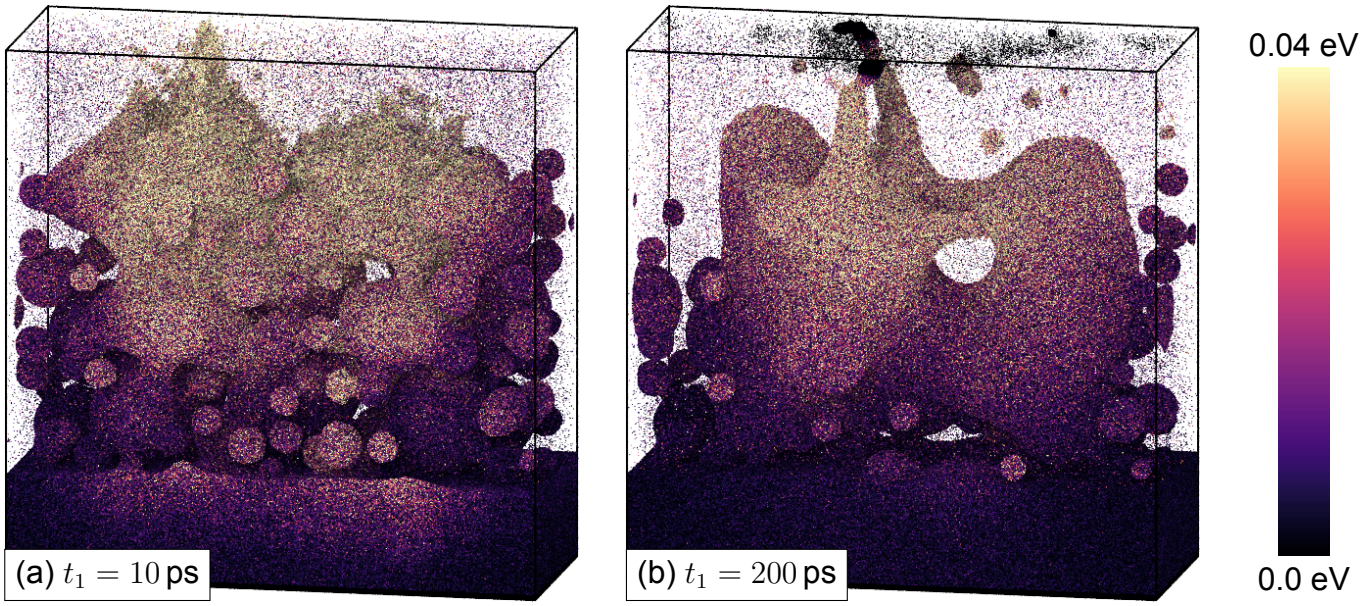

Figure 5.1: The heat distribution within the sample *coarse02* for two static laser beams penetration the sample past each other on different spots.

Bibliography

[1] Mohsen Attaran. The rise of 3-d printing: The advantages of additive manufacturing over traditional manufacturing. *Business Horizons*, 60(5):677–688, 2017.

[2] Lyle E Murr and et al. Metallic additive manufacturing: Current status and future prospects. *Materials Science and Engineering: R: Reports*, 74(1):171–206, 2012.

[3] Byron Blakey-Milner, Paul Gradl, Glen Snedden, Michael Brooks, Jean Pitot, Elena Lopez, Martin Leary, Filippo Berto, and Anton du Plessis. Metal additive manufacturing in aerospace: A review. *Materials Design*, 209:110008, 2021.

[4] Pinarello. Pinarello Bolide F10 Disk Frameset. `https://pinarello.com/global/en/bikes/road/competition/bolide-f-hr-3d`. Accessed: February 7, 2024.

[5] Galina Kasperovich and Joachim Hausmann. Improving fatigue performance of slm parts by surface modification. *Journal of Materials Processing Technology*, 220:202–214, 2015.

[6] Igor Yadroitsev and et al. Manufacture by selective laser melting and mechanical behavior of commercially pure titanium. *Materials Science and Engineering: A*, 593:170–177, 2014.

[7] Sebastian Kock and et al. Cost analysis of additive manufacturing. *Journal of Industrial Engineering International*, 13(4):541–550, 2017.

[8] Xiaodong Zhang and et al. Optimization of selective laser melting process parameters: A review. *Optics and Laser Technology*, 106:328–341, 2018.

[9] Dongdong Gu and et al. Virtual prototyping and optimization of selective laser melting for an aerospace component. *The International Journal of Advanced Manufacturing Technology*, 63(5-8):493–504, 2012.

[10] Johannes Roth, Eugen Eisfeld, Dominic Klein, Stephen Hocker, Hansjörg Lipp, and Hans-Rainer Trebin. Imd – the itap molecular dynamics simulation package. *The European Physical Journal Special Topics*, 227(14):1831–1836, Mar 2019.

[11] Dominic Klein. Laser ablation of covalent materials, 2023.

[12] Charles W. Hull. Apparatus for production of three-dimensional objects by stereolithography, 1986.

[13] Yong Lu and Jerry YH Fuh. Polyjet material jetting technology: A review. *Rapid Prototyping Journal*, 22(5):761–780, 2016.

[14] S. Scott Crump. Apparatus and method for creating three-dimensional objects, 1992.

[15] Emanuel Sachs, Michael Cima, James Cornie, and Paul Williams. Three-dimensional printing techniques, 1992.

[16] William E. Frazier. Metal additive manufacturing: A review. *Journal of Materials Engineering and Performance*, 23(6):1917–1928, Jun 2014.

[17] Alessandra Martucci, Alberta Aversa, and Mariangela Lombardi. Ongoing challenges of laser-based powder bed fusion processing of al alloys and potential solutions from the literaturemdash;a review. *Materials*, 16(3), 2023.

[18] Sagar Patel and Mihaela Vlasea. Melting modes in laser powder bed fusion. *Materialia*, 9:100591, 2020.

[19] S. Rahmati. 10.12 - direct rapid tooling. In Saleem Hashmi, Gilmar Ferreira Batalha, Chester J. Van Tyne, and Bekir Yilbas, editors, *Comprehensive Materials Processing*, pages 303–344. Elsevier, Oxford, 2014.

[20] Chao-Chen Li, Chun-Hsien Li, Shun-Chang Lin, Yu-Chen Su, Shan Jiang, Deng-Maw Lu, Jian-Ming Lu, Ming-Hsiao Lee, and Zhen Chen. Physical characteristics of nanoscale niobium-zirconium alloy powder during 3d printing laser sintering process — a molecular dynamics study. In *2018 IEEE International Conference on Applied System Invention (ICASI)*, pages 1322–1325, 2018.

[21] E.O. Olakanmi, R.F. Cochrane, and K.W. Dalgarno. A review on selective laser sintering/melting (sls/slm) of aluminium alloy powders: Processing, microstructure, and properties. *Progress in Materials Science*, 74:401–477, 2015.

[22] Dayong An, Yao Xiao, Xinxi Liu, Huan Zhao, Xifeng Li, and Jun Chen. Formation of two distinct cellular structures in 316l stainless steel fabricated by micro-laser beam powder-bed-fusion. *Materials Research Letters*, 12:42–49, 12 2023.

[23] J.P. Oliveira, A.D. LaLonde, and J. Ma. Processing parameters in laser powder bed fusion metal additive manufacturing. *Materials Design*, 193:108762, 2020.

[24] S. Tsukamoto. 2 - developments in co2 laser welding. In Seiji Katayama, editor, *Handbook of Laser Welding Technologies*, Woodhead Publishing Series in Electronic and Optical Materials, pages 17–46. Woodhead Publishing, 2013.

[25] Yi-Hsien Liu and Chung-Wei Cheng. The experimental and modeling study of femtosecond laser-ablated silicon surface. *Journal of Manufacturing and Materials Processing*, 7(2), 2023.

[26] Hardik Vaghasiya, Stephan Krause, and Paul-Tiberiu Miclea. Fundamental study of a femtosecond laser ablation mechanism in gold and the impact of the ghz repetition rate and number of pulses on ablation volume. *Opt. Mater. Express*, 13(4):982–996, Apr 2023.

[27] Joerg Schille, R. Ebert, Udo Loeschner, Patricia Scully, Nicholas Goddard, and Horst Exner. High repetition rate femtosecond laser processing of metals. *Proceedings of SPIE - The International Society for Optical Engineering*, 7589:21–, 02 2010.

[28] Lore Thijs, Karolien Kempen, Jean-Pierre Kruth, and Jan Van Humbeeck. Fine-structured aluminium products with controllable texture by selective laser melting of pre-alloyed alsi10mg powder. *Acta Materialia*, 61(5):1809–1819, 2013.

[29] M.A. Balbaa, A. Ghasemi, E. Fereiduni, M.A. Elbestawi, S.D. Jadhav, and J.-P. Kruth. Role of powder particle size on laser powder bed fusion processability of alsi10mg alloy. *Additive Manufacturing*, 37:101630, 2021.

[30] Jordan S. Weaver, Justin Whiting, Vipin Tondare, Carlos Beauchamp, Max Peltz, Jared Tarr, Thien Q. Phan, and M. Alkan Donmez. The effects of particle size distribution on the rheological properties of the powder and the mechanical properties of additively manufactured 17-4 ph stainless steel. *Additive Manufacturing*, 39:101851, 2021.

[31] Jincheng Wang, Rui Zhu, Yujing Liu, and Laichang Zhang. Understanding melt pool characteristics in laser powder bed fusion: An overview of single- and multi-track melt pools for process optimization. *Advanced Powder Materials*, 2(4):100137, 2023.

[32] Haijun Gong, Khalid Rafi, Hengfeng Gu, Thomas Starr, and Brent Stucker. Analysis of defect generation in ti–6al–4v parts made using powder bed fusion additive manufacturing processes. *Additive Manufacturing*, 1-4:87–98, 2014. Inaugural Issue.

[33] Xu Z.W., Qingyuan Wang, Xi-Shu Wang, C.H. Tan, M.H. Guo, and P.B. Gao. High cycle fatigue performance of alsi10mg alloy produced by selective laser melting. *Mechanics of Materials*, 148:103499, 06 2020.

[34] Alexander J. Dunbar, Erik R. Denlinger, Michael F. Gouge, and Pan Michaleris. Experimental validation of finite element modeling for laser powder bed fusion deformation. *Additive Manufacturing*, 12:108–120, 2016.

[35] Ruben Santamaria. *Molecular Dynamics*. Springer Cham, 2023.

[36] Rajendra R. Zope and Y. Mishin. Interatomic potentials for atomistic simulations of the ti-al system. *Phys. Rev. B*, 68:024102, Jul 2003.

[37] Message Passing Interface Forum. *MPI: A Message-Passing Interface Standard Version 2.2*, June 2021.

[38] Azad Gorgis. Simulation studies of selective laser melting, September 2022.

[39] Azad Gorgis. Additive manufacturing of binary alloys, September 2023.

[40] Pranitha Sankar and Reji Philip. Chapter 11 - nonlinear optical properties of nanomaterials. In Sneha Mohan Bhagyaraj, Oluwatobi Samuel Oluwafemi, Nandakumar Kalarikkal, and Sabu Thomas, editors, *Characterization of Nanomaterials*, Micro and Nano Technologies, pages 301–334. Woodhead Publishing, 2018.

[41] P. Drude. Zur elektronentheorie der metalle. *Annalen der Physik*, 306(3):566–613, 1900.

[42] J. P. Girardeau-Montaut, M. Afif, C. Girardeau-Montaut, S. D. Moustaïzis, and N. Papadogiannis. Aluminium electron-phonon relaxation-time measurement from subpicosecond nonlinear single-photon photoelectric emission at 248 nm. *Applied Physics A*, 62(1):3–6, Jan 1996.

[43] Beer. Bestimmung der absorption des rothen lichts in farbigen flüssigkeiten. *Annalen der Physik*, 162(5):78–88, 1852.

[44] S. Sonntag, C. Trichet Paredes, J. Roth, and H.-R. Trebin. Molecular dynamics simulations of cluster distribution from femtosecond laser ablation in aluminum. *Applied Physics A*, 104(2):559–565, Aug 2011.

[45] Fabio Oelschläger. Molekulardynamische simulation von selektivem laserschmelzen, April 2021.

[46] J. Dana. Honeycutt and Hans C. Andersen. Molecular dynamics study of melting and freezing of small lennard-jones clusters. *The Journal of Physical Chemistry*, 91(19):4950–4963, Sep 1987.

[47] Zbigniew D Jastrzebski and Ranga Komanduri. The nature and properties of engineering materials. 1959.

[48] Pauli Virtanen, Ralf Gommers, Travis E. Oliphant, Matt Haberland, Tyler Reddy, David Cournapeau, Evgeni Burovski, Pearu Peterson, Warren Weckesser, Jonathan Bright, Stéfan J. van der Walt, Matthew Brett, Joshua Wilson, K. Jarrod Millman, Nikolay Mayorov, Andrew R. J. Nelson, Eric Jones, Robert Kern, Eric Larson, C J Carey, İlhan Polat, Yu Feng, Eric W. Moore, Jake VanderPlas, Denis Laxalde, Josef Perktold, Robert Cimrman, Ian Henriksen, E. A. Quintero, Charles R. Harris, Anne M. Archibald, Antônio H. Ribeiro, Fabian Pedregosa, Paul van Mulbregt, and SciPy 1.0 Contributors. SciPy 1.0: Fundamental Algorithms for Scientific Computing in Python. *Nature Methods*, 17:261–272, 2020.

[49] Han Wang, Carsten Hartmann, Christof Schütte, and Luigi Delle Site. Grand-canonical-like molecular-dynamics simulations by using an adaptive-resolution technique. *Phys. Rev. X*, 3:011018, Mar 2013.

[50] Simon Pauly, Pei Wang, Uta Kühn, and Konrad Kosiba. Experimental determination of cooling rates in selectively laser-melted eutectic al-33cu. *Additive Manufacturing*, 22:753–757, 2018.

[51] Bo Cheng and Kevin Chou. Melt pool evolution study in selective laser melting. 08 2015.

[52] Quanquan Han, Rossitza Setchi, and Sam L. Evans. Characterisation and milling time optimisation of nanocrystalline aluminium powder for selective laser melting. *The International Journal of Advanced Manufacturing Technology*, 88(5):1429–1438, Feb 2017.

[53] Ravindranadh Bobbili, Vemuri Madhu, and Ashok Kumar Gogia. Tensile behaviour of aluminium 7017 alloy at various temperatures and strain rates. *Journal of Materials Research and Technology*, 5(2):190–197, 2016.

[54] D. Fisher, M. Fraenkel, Z. Henis, E. Moshe, and S. Eliezer. Interband and intraband (drude) contributions to femtosecond laser absorption in aluminum. *Phys. Rev. E*, 65:016409, Dec 2001.

[55] Li-li Zhou, Jia-ming Pan, Lin Lang, Ze-an Tian, Yun-fei Mo, and Ke-jun Dong. Atomic structure evolutions and mechanisms of the crystallization pathway of liquid al during rapid cooling. *RSC Adv.*, 11:39829–39837, 2021.

[56] Jiaxin Lv, Jing-Hua Zheng, Victoria A. Yardley, Zhusheng Shi, and Jianguo Lin. A review of microstructural evolution and modelling of aluminium alloys under hot forming conditions. *Metals*, 10(11), 2020.

[57] Sachin Kurian and Reza Mirzaeifar. Selective laser melting of aluminum nano-powder particles, a molecular dynamics study. *Additive Manufacturing*, 35:101272, 2020.

[58] Naijia Liu, Tianxing Ma, Chaoqun Liao, Guannan Liu, Rodrigo Miguel Ojeda Mota, Jingbei Liu, Sungwoo Sohn, Sebastian Kube, Shaofan Zhao, Jonathan P. Singer, and Jan Schroers. Combinatorial measurement of critical cooling rates in aluminum-base metallic glass forming alloys. *Scientific Reports*, 11(1):3903, Feb 2021.

[59] Qiang Zeng, Lijuan Wang, and Wugui Jiang. Molecular dynamics simulations of the tensile mechanical responses of selective laser-melted aluminum with different crystalline forms. *Crystals*, 11(11), 2021.

[60] Yudi Rosandi, Hoang-Thien Luu, Herbert M. Urbassek, and Nina Gunkelmann. Molecular dynamics simulations of the mechanical behavior of alumina coated aluminum nanowires under tension and compression. *RSC Adv.*, 10:14353–14359, 2020.

Danksagung

An dieser Stelle möchte ich mich bei Professor Roth für die geduldige Betreueung, große Hilfsbereitschaft und den guten Input zu meiner Arbeit bedanken. Des weitern danke ich meinem Mitberichter Professor Holm für die Gespäche über die Arbeit, die mich dazu bewegt haben einige Hintergründe noch einmal genauer aufzuarbeiten.
Zudem möchte ich mich bei allen Freunden die mir immer Rückhalt gegeben haben und Bekanntschaften, die ich während des Studiums gemacht habe Bedanken.
Der größte Dank geht an meine Eltern, die mich die letzen sechs Jahre unterstützt haben und ohne die ein erfolgreiches Studium nicht möglich gewesen wäre.

Jonas Schmid

Eidesstattliche Erklärung

Hiermit erkläre ich, dass ich die vorliegende Arbeit eigenständig und ohne fremde Hilfe angefertigt habe. Textpassagen, die wörtlich oder dem Sinn nach auf Publikationen oder Vorträgen anderer Autoren beruhen, sind als solche kenntlich gemacht. Die Arbeit wurde bisher keiner anderen Prüfungsbehörde vorgelegt und auch noch nicht veröffentlicht.

_____ Date: 12. März 2024

Jonas Schmid